

General Disclaimer

One or more of the Following Statements may affect this Document

- This document has been reproduced from the best copy furnished by the organizational source. It is being released in the interest of making available as much information as possible.
- This document may contain data, which exceeds the sheet parameters. It was furnished in this condition by the organizational source and is the best copy available.
- This document may contain tone-on-tone or color graphs, charts and/or pictures, which have been reproduced in black and white.
- This document is paginated as submitted by the original source.
- Portions of this document are not fully legible due to the historical nature of some of the material. However, it is the best reproduction available from the original submission.

Raul G. ... 224.5

SU-SEL-69-066

Stanford Telemetry Monitoring Experiment on Lunar Explorer 35

by

G. L. Tyler

D. H. H. Ingalls

R. A. Simpson

October 1969

Final Report

Prepared under

National Aeronautics and Space Administration
Contract NAS5-9347

N70-20473

(ACCESSION NUMBER)

86

(PAGE)

CR#108901

(NASA CR OR TMX OR AD NUMBER)

(THRU)

1

(CODE)

30

(CATEGORY)



IOSCIENCE LABORATORY

STANFORD ELECTRONICS LABORATORIES

STANFORD UNIVERSITY • STANFORD, CALIFORNIA



FACILITY FORM 602

SEL-69-066

STANFORD TELEMETRY MONITORING EXPERIMENT ON LUNAR EXPLORER 35

by

G. L. Tyler
D. H. H. Ingalls
R. A. Simpson

October 1969

Final Report

Prepared under

National Aeronautics and Space Administration
Contract NAS5-9347

Radioscience Laboratory
Stanford Electronics Laboratories
Stanford University Stanford, California

PRECEDING PAGE BLANK NOT FILMED.

CONTENTS

	<u>Page</u>
I. INTRODUCTION	1
II. SUMMARY DESCRIPTION OF THE EXPERIMENT	5
III. MEASUREMENT PROCEDURES	15
IV. SCIENTIFIC RESULTS	19
V. DATA ACQUISITION	23
VI. REDUCTION AND ANALYSIS OF ECHO DATA	25
A. Data Reduction	25
B. Measurements of Surface Reflectivity	25
C. Measurement of Slopes	26
VII. OCCULTATIONS	27
A. Occultation Data Acquisition	28
B. Occultations: Data Reduction	29
C. Occultations: Analysis	31
VIII. CONCLUSIONS	37
APPENDIX	39
BIBLIOGRAPHY	79

PRECEDING PAGE BLANK NOT FILMED.

ILLUSTRATIONS

<u>Figure</u>	<u>Page</u>
1. Experimental geometry for Explorer 35 experiments	5
2. Normalized bistatic radar cross section	9
3. Distribution of Explorer 35 bistatic radar data points	17
4. Outline of data processing for occultation observations	30
5. Side view of the Explorer 35 spacecraft (not to scale) showing measurement of the polar angle θ	40
6. Top view of the Explorer 35 spacecraft (not to scale)	40
7. Orientation of a small current element in xyz space	41
8. A current rod of arbitrary length d can be approximated by a sum of smaller current elements	42
9. An observer will detect an electric field \bar{E}_θ from a current element	44
10. Linear and circular radiation patterns of the ideal antenna model at a polar angle of $\theta = 60^\circ$	47
11. Linear and circular radiation patterns of the ideal antenna model in the equatorial plane $\theta = 90^\circ$	48
12. Spacecraft linear and circular radiation patterns measured by GSFC at a polar angle $\theta = 60^\circ$	49
13. Spacecraft linear and circular radiation patterns measured by GSFC in the equatorial plane $\theta = 90^\circ$	50
14. Scaling functions used to compensate for distortion by solar panels and magnetometer booms	51
15. Circular radiation pattern from the θ -scaled antenna model at an angle of $\theta = 60^\circ$	52
16. Circular radiation pattern from the θ -scaled antenna model in the equatorial plane $\theta = 90^\circ$	53
17. Ratio of measured total circular to total linear power taken from the GSFC-supplied patterns at all polar and rotational angles	54
18. Variance plotted against angle as the circular patterns are rotated relative to the linear patterns	56

ILLUSTRATIONS (Cont)

<u>Figure</u>	<u>Page</u>
19. Best offset angle as a function of θ	58
20. Circular radiation pattern calculated for the array-scaled model at $\theta = 60^\circ$	59
21. Circular radiation pattern calculated for the array-scaled model in the equatorial plane $\theta = 90^\circ$	59
22. The polarization ellipse showing quantities of interest	60
23. θ and ϕ contributions add to give a total left circular vector	62
24. θ and ϕ contributions add to give a total right circular vector	62
25. \bar{E}^L and \bar{E}^R coincide at γ_0 to produce the maximum electric vector \bar{E}_m	63
26. From the lunar equator Explorer 35 appears to rise in the east with spin vector \bar{S} pointed generally south	65
27. The spacecraft appears to set in the west with the spin vector still pointing south	66
28. Poincaré power parameter S_0 plotted against rotation angle for both the ideal and array-scaled models	68
29. χ vs right minus left circular powers in decibels for the ideal model	69
30. χ vs right minus left circular powers in decibels for the array-scaled model	70
31. Variations in χ for the ideal and array-scaled models over 90° of spacecraft rotation	71
32. γ_0 vs ϕ minus θ linear powers in decibels for the array-scaled model	72
33. γ_0 vs ϕ minus θ linear powers in decibels for the ideal model	73
34. Variation in γ_0 as the spacecraft rotates over 90°	74
35. Average Poincaré parameters and Poincaré parameters for average fields	75

ILLUSTRATIONS (Cont)

<u>Figure</u>		<u>Page</u>
36.	Average S_0 over 360° of rotation with error bars indicating the maximum deviation from this value when an average over only 150° is taken	76
37.	Average γ_0 over 360° of rotation showing deviation when 150° average is used	77
38.	Average χ over 360° of rotation showing deviation when 150° average is used	78

I. INTRODUCTION

Lunar Explorer 35 (also Anchored-IMP) is a small spin-stabilized spacecraft designed and constructed by Goddard Space Flight Center (GSFC) and placed in a lunar orbit on July 22, 1967. The instrument complement was selected to provide detailed information on the particles and electromagnetic fields in the vicinity of the moon and includes plasma probes, cosmic dust detectors, magnetometers and energetic particle detectors. Data from these experiments are transmitted to earth over a 136 MHz (2.2 m) telemetry system which radiates approximately 6 watts through an omnidirectional antenna system.

The Stanford Telemetry Monitoring Experiment utilizes the telemetry transmissions from the spacecraft to conduct bistatic-radar* studies of the lunar surface. A portion of the signals radiated from the spacecraft strike the moon and are scattered toward the earth. These echo signals are received on the ground and, providing certain prerequisite conditions are met, separated from the much stronger directly propagating waves which they accompany. Variations in the strength and spectral characteristics of the echoes are then interpreted as resulting from variations in lunar surface structure and material.

These observations represent the first systematic, scientific investigation of an extra-terrestrial body using these techniques. Bistatic-radar echoes from the lunar surface had been previously detected, both in the Soviet Union by Yakovlev et al. [1968] and at about the same time by members of the group which conducted the present experiment at Stanford [Tyler et al., 1968]. At Stanford, this work was the outgrowth of the progressive application of radio links to the study of remote objects, and grew naturally out of previous work.

The following goals were among the scientific aims of this experiment:

* The terminology "bistatic-radar" implies active radio frequency sounding using well separated transmitter and receiver.

- (1) To separate the effects of lunar surface shapes from those of the material composition;
- (2) To unambiguously determine the bulk electromagnetic properties of the lunar crust;
- (3) To partially resolve ambiguities in earth based observations of variations (i.e., deviations from the average) in lunar electromagnetic properties in terms of the regional geological structure of the moon;
- (4) To study the properties of the lunar limb as a diffracting edge in occultation.

Almost all of these goals were achieved, with the principal exception of four where it is still not entirely clear whether or not the telemetry carrier is sufficiently unaffected by low-frequency components of the telemetry modulation system to permit the necessary data analysis to be carried out. The scientific results of this experiment are discussed in Section IV of this report.

Observations were carried out at Stanford and at the Arecibo Ionospheric Observatory. All the data from the Stanford observations have been reduced and are in a form suitable for analysis. At the time of this writing the Arecibo data are only partially reduced.

Analysis of reflectivity data is dependent upon accurate knowledge of the spacecraft trajectory, orientation, and antenna patterns. This information was supplied in support of the experiment by GSFC.

There have been a number of publications, both in the form of scientific papers and technical reports, relating to the telemetry monitoring experiment. Reports describing the telemetry receiving system, data reduction, and the necessary orbital computations are available to interested readers. Scientific publications appear in the literature.

This report is intended to provide a technical record of the experiment. Consequently, all the major aspects of the work will be discussed. However, in the case of information which has already appeared elsewhere discussion will be brief, with appropriate references. Two major areas which have not appeared previously are those of the occultation studies and the resolution of certain problems in interpretation of the GSFC antenna patterns. Both of these topics are discussed at some length,

primarily because they may bear heavily upon future scientific interpretation of some of the results, and also because they required a considerable effort to understand.

Analysis of the Explorer 35 data and its relation to previous radar studies is continuing with further support from NASA.

PRECEDING PAGE BLANK NOT FILLED.

II. SUMMARY DESCRIPTION OF THE EXPERIMENT

The orbit of Explorer 35 lies in a plane which is roughly parallel to the lunar equator, varies between 700 and 7000 km in altitude above the lunar surface, and has a period very nearly equal to 11.5 hr. Figure 1 is a representation of the experimental geometry, with the spacecraft

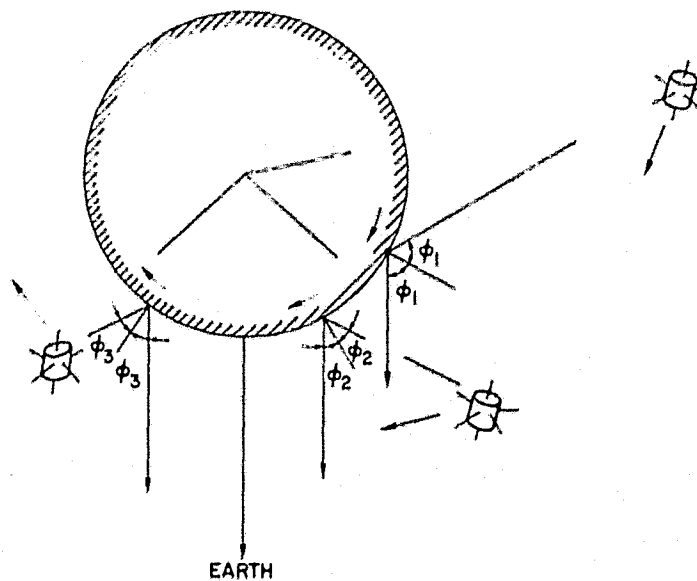


Fig. 1. EXPERIMENTAL GEOMETRY FOR EXPLORER 35 EXPERIMENTS.

shown in three successive positions of its motion about the moon. At each position the plane of the figure is that which contains the center of mass of the moon, the spacecraft, and the earth-bound observer. With the orbital parameters given above the spacecraft may be within 0.4 lunar radii of the surface, or as far away as 4.0 lunar radii from the surface. The position of the observer with respect to these maxima and minima varies with the lunar cycle as the orbit, which may be considered fixed in inertial space, is carried about the earth by the motion of the moon.

Consider, for the moment, the case of a perfectly smooth moon. The rays drawn (in Fig. 1) from the spacecraft to the surface represent that portion of the radiated energy which is specularly scattered toward the earth, i.e., reflected from a Fresnel size area about the locations on the surface where the angle of incidence and reflection are equal. This location is the center of the first Fresnel zone on the surface, and is

referred to as the specular point, whereas the angle is referred to as the angle of incidence. The angle ϕ must be nearly equal to the lunar longitudes of the specular points at times when the spacecraft and the earth lie in the equatorial plane of the moon. In this case, the only discrepancies between the two angles, lunar longitude and ϕ , would be due to the libration in longitude of the moon. Since the libration is usually only a few degrees and since Explorer 35 is in a roughly equatorial orbit, we are sufficiently close to the case where the angle of incidence equals the selenographic longitude to use this equivalence as a convenient mechanism for visualizing the experimental geometry.

There are three intrinsic experimental parameters which influence the strength of the echo from a smooth sphere: the reflectivity of the lunar surface averaged over the reflecting region, the mean curvature imparted to the wavefront of the reflected wave by the spherical geometry of the moon, and the altitude of the spacecraft above the surface.

In the radar equation given below, the effects of these parameters on the total received power is multiplicative. We have

$$P_R = \frac{P_T G_T A_R}{(4\pi)^2 R_E^2} \cdot \sigma_\beta \cdot \frac{1}{R_S^2} \cdot |\rho|^2 \quad (1)$$

where P_R = received power

P_T = transmitted power

G_T = gain of transmitting antenna

A_R = effective area of receiving antenna

R_E = distance from the center of the moon to the observer

These first five factors have been isolated since they are generally fixed for a given set of observations. The three remaining factors are the intrinsic parameters mentioned above which may vary considerably.

They are:

σ_{β} = bistatic radar cross section of a smooth conducting sphere the size of the moon

ρ = complex voltage reflection coefficient of the lunar surface

R_s = distance from the center of the moon to the space probe

The principal geometric effects of the spherical geometry are incorporated in the bistatic radar cross section of a conducting sphere σ_{β} .

In practice, however, the reflection comes not from a point, as indicated in Fig. 1, but from a glistening region of specular points or glints surrounding the point of specular reflection on the mean surface. To the first order, this reflecting region consists of the fraction of the surface where it is likely, in a probabilistic sense, that large areas will have the tilts or slopes required for the production of a specular reflection in the direction toward the observer. In the case of a completely smooth moon, there would exist simply a single bright spot of Fresnel-zone size centered on the specular point. Replacement of a completely smooth sphere by a moon with a gently undulating surface causes the Fresnel zone to be broken into a group of many smaller spots, but in such a way that on the average the total reflected power is essentially unaffected. This result has been derived for the special case of backscatter by Hagfors [1968] and for the bistatic-radar or oblique scatter case by Fjeldbo [1964].

Students of electromagnetic scattering from surfaces distinguish between two very different phenomena, referred to as "specular," or "quasi-specular" reflections and "diffuse" scattering. Observationally, quasi-specular reflections are deterministically polarized and sharply peaked (in strength) in the specular direction as determined by the mean reflecting surface. Diffuse scattering is characterized by a randomness of phase and polarization characteristics (over an ensemble of surfaces, or over different portions of the same surface) and a very broad spatial distribution of power. It is the quasi-specular component of the scattering which is observed here.

Fjeldbo's results depend upon the Huygens-Kirchhoff approximation and apply to a body of many wavelengths in diameter whose mean surface is spherical but whose true surface deviates from the mean according to

gaussian statistics. When the observer is much farther from the scattering body than the probe, one has

$$\sigma_{\beta} = \frac{4\pi \cos\theta R_s^2}{\left(\cos\theta + \frac{2d}{R_p}\right)\left(1 + \frac{2d \cos\theta}{R_p}\right)} \quad (2)$$

The new quantities in this expression, d and R_p , are the distance from the specular point on the mean surface to the spaceprobe and the radius of the scattering body, respectively. This is precisely the expression for the bistatic-radar cross section of a smooth sphere [van der Pol and Bremmer, 1937], showing that the cross section is unaffected by first order roughness. For the backscatter case, $\theta = 0$, σ_{β} varies from $4\pi R_p^2$ to πR_p^2 as R_s goes from R_p to infinity. This corresponds to a change in the radar cross section from that of a flat plate to that of a sphere at infinity. For a constant radius R_s , the cross section monotonically decreases from a maximum at $\theta = 0$ until it vanishes at $\theta = \pi/2$. In general, however, a given change in R_s may either increase or decrease σ_{β} , depending on the value of θ . This function is illustrated in Fig. 2.

Hagfors [1968], in a more complete analysis of the special case of backscatter ($\theta = 0$, $R_s = R_E$), concluded that the cross section of a sphere is increased by a small amount when roughness is present. The correction factor derived by Hagfors is $1 + K_i(\alpha)^2$, where α is the rms slope of the surface and K_i is a constant which depends upon the stochastic process used as a model. The product $K_i(\alpha)^2$ is always much less than unity. For a gaussian surface, $K_i = 1$.

In general, the monostatic radar observations, the Lunar-Orbiter photographs, and the roughness measurements of this experiment all indicate that on a scale of meters the lunar surface is quite smooth with an average slope of less than 5° . Slopes of this magnitude imply that the glistening region is on the order of 150 to 200 km in diameter, or about the size of the crater Copernicus and its immediate, hummocky environs. For the observations reported here, the distance from the center of the moon to the spacecraft was usually less than two lunar radii. The close

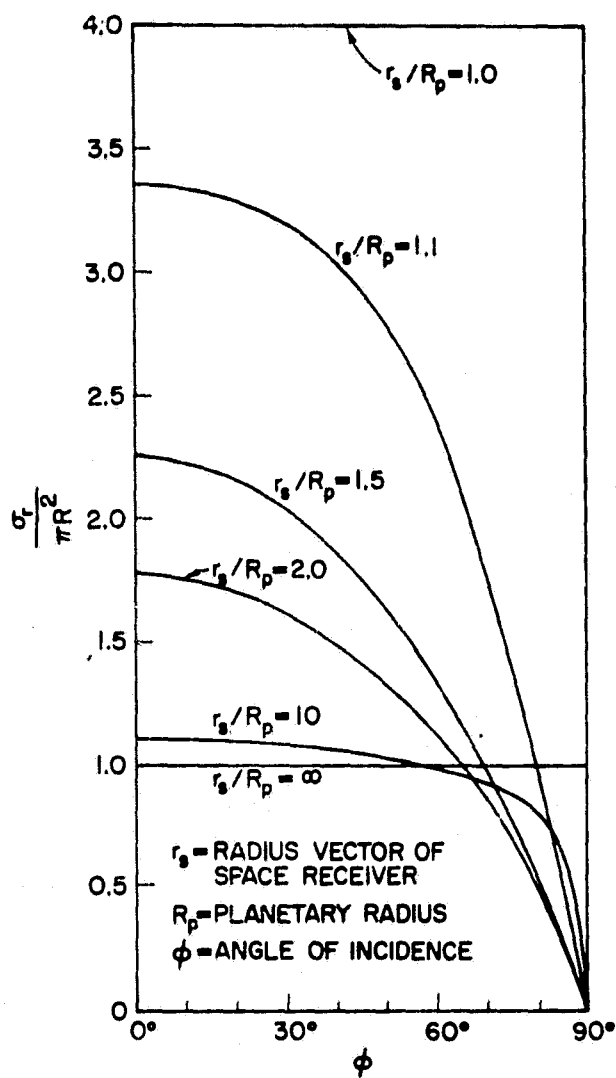


Fig. 2. NORMALIZED BISTATIC RADAR CROSS SECTION.

proximity to the surface accounts for the somewhat smaller spot size than that which would be observed when using a transmitter at a higher altitude. Hagfors' correction term is about 1 percent, depending on the model chosen. There may exist mechanisms involving small scale roughness of the surface that will modify these results, but at present this does not appear to be the case.

It is well known in the theory of scattering that, when given the types of surfaces under consideration here, the principal component of the scattered wave arises from those portions of the surface which are properly oriented to produce a mirror-like reflection toward the observer. In the case of quasi-specular reflection, almost all of the scattered energy comes from the fractions of the surface whose radii of curvature are very large with respect to a wavelength and whose tangent planes are very

nearly parallel to the mean surface at the center of the reflecting area. Thus, to a good approximation the appropriate reflection coefficient ρ is that of a plane wave on a plane surface of large extent. The power reflection coefficient is given then by the squared modulus of the appropriate Fresnel coefficient, or in the case of complicated incident polarization, by the application of the Fresnel coefficients to the individual components of the incident wave. Conversely, a measurement of reflectivity may be interpreted as the reflection from a smooth plane interface. Since the Fresnel coefficients are very well known, they will not be discussed here.

The final variable term of importance to the experiment is the space-attenuation factor involving R_s . Expression 2 for σ_β was derived using the moon center for probe distance in the radar equation, so this is the proper value to use. But, since this is simply the radius of the orbit, it may also be obtained from the known orbital parameters.

The lunar surface reflectivity is obtained by measuring the total reflected power and then correcting for the known geometrical effects, as expressed in σ_β and $1/R_E^2$, and for the instrumentation and moon-earth path loss effects as expressed in the grouped factors in radar Eq. 1. For the purposes of this report, the procedure just described is taken as an operational definition of the power reflection coefficient. Variations in surface roughness hardly affect the results since the total forward scattered power is almost independent of surface roughness. The reader should be careful to distinguish the present case from the power scattered per unit area, which does not display a similar independence of surface shape.

If the moon were a perfectly smooth sphere, the spectrum of the echo signal would mirror that of the direct signal; however, departures of the lunar surface from a simple, smooth geometrical shape, coupled with the relative motion of the bodies involved, modulate the reflected wave, causing it to be broadened in frequency. The extent of this frequency broadening is directly related to the statistics of the surface.

The autocorrelation function for the actual surface may be written as

$$\langle h(u, w) \cdot h(u + \Delta u, w + \Delta w) \rangle = h_o^2 \rho(r) \quad (3)$$

where $r^2 = \Delta u^2 + \Delta w^2$ and $\langle h \rangle = 0$. The coordinates (u, w) represent a local orthogonal system in a plane tangent to the mean surface at the point of interest. Fjeldbo finds the envelope of the autocorrelation function of the received echo signal to be

$$R(\tau) = R(0) \exp \left\{ -16\pi^2 \frac{h_o^2}{\lambda^2} \cos^2 \phi [1 - \rho(v\tau)] \right\} \quad (4)$$

where λ = the free space wavelength at the center frequency of the reflected signal,

v = the velocity of the center of the first Fresnel zone on the mean surface,

τ = time lag at which the autocorrelation function is calculated

ϕ = the angle of incidence at the center of the first Fresnel zone on the mean surface, and

$R(0)$ = total reflected power.

For a surface autocorrelation function of the form

$$\rho(v\tau) = 1 - \left(\frac{v\tau}{L} \right)^2 \quad (5)$$

with $\phi = 0$, (4) reduces to Hagfors' [1961] expression for a similar function in backscatter.

If $16\pi^2 \cdot h_o^2 / \lambda^2 \cdot \cos^2 \phi \gg 1$, as it is for the moon at 2 m wavelengths, the behavior of $R(\tau)$ is determined by the behavior of $\rho(v\tau)$ near the origin since the exponential will decay very rapidly with a decrease in $\rho(v\tau)$. Then $R(\tau)$ varies as

$$R(\tau) \propto \exp \left\{ -4k^2 v^2 \cos^2 \phi \left[-\frac{h_o^2}{2} \rho''(0) \right] \tau^2 \right\} \quad (6)$$

where $\rho''(0) = d^2\rho(0)/dr^2$ and $k = 2\pi/\lambda$. We have used a Taylor series expansion to approximate $\rho(v\tau)$ near the origin and have assumed that the first derivative is zero. The power spectrum is related to $R(\tau)$ by the Fourier transform. Thus

$$S(f) = \exp \left\{ -\pi^2 f^2 \left[4k^2 v^2 \cos^2 \theta \left(-\frac{h_o^2}{2} \rho''(0) \right) \right]^{-1} \right\} \quad (7)$$

The one-half power bandwidth is given by

$$\Delta f = 4(2 \cdot \ln 2)^{1/2} \frac{v}{\lambda} \cos \theta h_o [-\rho''(0)]^{1/2} \quad (8)$$

Clearly, a real surface containing rocks, boulders, fissures and cliffs is not well approximated by the smooth, gently undulating model used here. However, there seems to be general agreement in the literature that such an analysis is valid for the quasi-specular component of reflection, provided the results are interpreted as being measures of surface properties over a scale range related to the probing wavelength and the angle of incidence. This problem has been considered by at least one author [Hagfors, 1966] but there are few or no quantitative results available. As a lower bound, structure on the scale of a few wavelengths will begin to scatter diffusely. As an absolute upper bound, structures larger than a Fresnel zone will scatter with roughly uniform effectiveness. This argument leads to an estimate of effective lateral scales between ten and several hundred meters for the present experiment. Most likely some sort of average over this range of sizes is called for.

For a gaussian autocorrelation function such as

$$\rho(r) = \exp\left(-r^2/2d_o^2\right) \quad (9)$$

the quantity $-h_o^2 \rho''(0) = h_o^2/d_o^2$ is directly related to surface slopes [Middleton, 1960]. Following Hagfors [1966], the unidirectional rms slope in any direction along the surface is given by

$$\langle t_u^2 \rangle^{1/2} = \langle t_w^2 \rangle^{1/2} = \frac{h_o}{d_o} \quad (10)$$

where $t_u = \partial h / \partial u$ and $t_w = \partial h / \partial w$ are the first partial derivatives of the surface height deviations in two orthogonal directions along the surface. The mean slope as determined by the tangents of the angles ψ between the local surface normals and the normal to the mean surface is given by

$$\langle \tan \psi \rangle = \left(\frac{\pi}{2} \right)^{1/2} \frac{h_o}{d_o} = 1.25 \frac{h_o}{d_o} \quad (11)$$

while the rms value is given by

$$\langle \tan^2 \psi \rangle^{1/2} = 2^{1/2} \frac{h_o}{d_o} = 1.41 \frac{h_o}{d_o} \quad (12)$$

PRECEDING PAGE BLANK NOT FILMED.

III. MEASUREMENT PROCEDURES

Transmissions from Explorer 35 are on a center frequency of 136.11 MHz, or approximately 2.2 m wavelength. The total radiated power is about 6.0 W, of which only the 2.0 W residing in the telemetry carrier are useful for the purposes of this experiment. The remaining 4.0 W appear in the spacecraft telemetry sidetones, which symmetrically occupy the frequency spectrum from 275 to 937 Hz on both sides of the telemetry carrier. The reflected signal generally is offset in frequency from the spacecraft carrier by the doppler effect operating through the difference in the rate of change of the direct and reflected paths. Useful observations may be accomplished during those periods when the doppler offset causes the reflected signal to fall into the clear region of the spectrum between the carrier and the sidetones. The doppler offsets, however, are never sufficient to carry the reflection clear of the direct signal on the outside of the sidetones. In addition, there are brief periods during tracking operations when the telemetry sidetones are absent, so that observations can be made in the otherwise forbidden region of the spectrum.

The data for this experiment are principally received at Stanford University with the 150-ft Stanford Research Institute dish antenna where they are analog recorded for subsequent sampling and digital spectral analysis. The reflected signal usually is identified easily in the frequency domain. A comparison of the observed time-frequency trajectories of the reflections with those predicted from the orbital parameters is employed as a safeguard against errors.

If the moon were the perfectly smooth sphere we have postulated in our previous discussion, the reflected signal would appear as simply an attenuated version of the telemetry carrier displaced in frequency. However, because of the roughness of the lunar surface, there exists not one but a multiplicity of radio images of the spacecraft on the moon, one from each properly oriented facet of the surface. Since these images all form slightly different angles with respect to the velocity vector of the vehicle, they represent slightly different doppler shifts, thus producing the noise-like, spectrally broadened composite of the reflected carrier signal whose statistics we have discussed above. The total received power is obtained by integration of that portion of the frequency spectrum

containing the reflected signal and subtraction of the fraction of the integral attributable to system noise. Spectral characteristics of the reflected signal will be the subject of additional work.

Radiation from the spacecraft takes place through a modified turnstile antenna whose elements divide a cone of included half-angle equal to 75° into four equal segments, and whose axis is coincident with the vehicle spin axis. The elements are driven in phase quadrature with the result that the radiated polarization is circular on the spin axis, with reversed sense of rotation in the two opposite directions of propagation. There is a small region roughly normal to the spin axis where the radiated polarization is linear. Between these two extremes, the polarization is elliptical. Consequently, the polarization of the illuminating wave may change considerably from one part of an orbit to the next, and from day to day. Right and left circular polarizations are received on the ground to accommodate the wide range of possible radiated polarizations and to avoid the effects of Faraday rotation in the earth's ionosphere.

Observations were carried out over a fraction of the spacecraft orbit on a number of separate occasions. Thus, during a single observing period the reflecting area would traverse a path across the disk according to the law of specular reflection on the mean surface. Data were taken in the form of analog tape recordings of the receiver output for subsequent digital sampling and spectral analysis. The spectral analysis programs employed a sine-squared data weighting with coherent integration periods of 1 or 2 sec. Since the sine-squared weighting halves the effective integration time, the corresponding analysis bandwidths were approximately 2 and 1 Hz, respectively. Smoothing of the spectral estimates was accomplished by summing 60 to 120 successive square magnitudes of the Fourier coefficients in time and four adjacent frequencies. The longer integration periods were required when the spacecraft was near apoapsis or the reflecting area was near the limb of the moon since the reflected signals were quite weak in both of these cases.

Figure 3 is a plot, in selenographic coordinates, of the position of the reflecting area at the midpoint of the incoherent integration periods. Each letter represents observations from a different orbit so that the track of the reflecting area may be followed across the disk. The

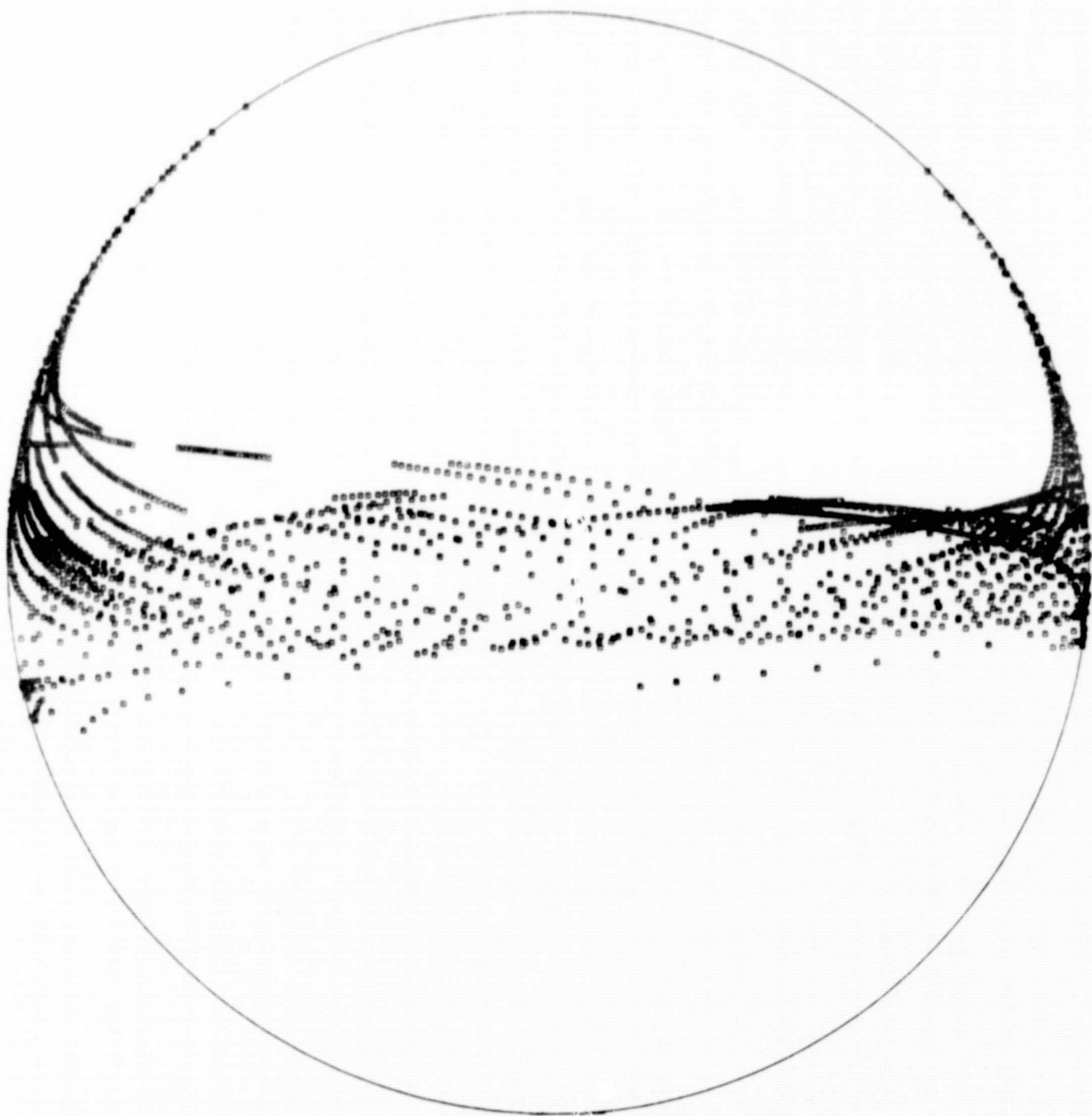


Fig. 3. DISTRIBUTION OF EXPLORER 35 BISTATIC RADAR DATA POINTS.

noticeable thinning of data tracks near the center of the disk is a result of the differential doppler restrictions imposed by the telemetry sidebands.

PRECEDING PAGE BLANK NOT FILMED.

IV. SCIENTIFIC RESULTS

Thus far the work described in this report has resulted in the publication of three scientific papers regarding the nature and electromagnetic properties of the lunar surficial layer [Tyler, 1968a,b and Tyler and Simpson, 1970]. The experimentally derived properties of the lunar surface at 2.2 m are listed below.

- (a) The relative dielectric constant of the bulk lunar surface in the southwestern portion of Oceanus Procellarum is 3.0 ± 0.2 as determined from the Brewster angle of the lunar crust.
- (b) The quasi-specular portion of forward scattered echoes from the lunar surface is roughly 30 percent greater for maria than for highland regions.
- (c) Large variations (2:1 normalized to the expected echoes from plane dielectric with $\epsilon_r = 3.0$) in quasi-specular reflectivity occur within Oceanus Procellarum in the rill region east of the Flamsteed ring.
- (d) The lunar surface, on a scale of 100 m, is extremely smooth with unidirectional rms slopes of 2° , 3° , and 6° for Mare Fecunditatis and Oceanus Procellarum, the central highlands and terra surrounding the crater Alfraganus, and the Censorinus highlands, respectively.

These results have significant implications for the interpretation of lunar radar observations; consideration of these is in the order presented above.

- (a) Dielectric Constant of the Lunar Crust. It is now clear from laboratory results [Campbell et al., 1969] that the relative dielectric constant of geophysical material is primarily a measure of the density of that material. Prior to the Explorer 35 experiment the best ground based radar estimates, based on the total lunar radar cross section, led to values of relative dielectric constant of 2.7 to 2.8 at centimeter wavelengths. A number of assumptions as to the scattering behavior of the lunar surface were required and this result was in considerable disagreement with the radiometrically determined value of 1.7. It was not clear where the difficulty lay. Detection of the Brewster null in the bistatic experiment constitutes a direct measure of dielectric constant. Within the experimental errors the value determined in this work and inferred from the total cross section are in agreement. The slight discrepancy may be due to a wavelength dependence in the electromagnetic properties

of the surface. It now seems clear that the interpretation given to the quasi-specular component of the earth based and bistatic observations, viz: that this component arises from large, nearby plane segments of the surface whose reflectivity is given by the appropriate Fresnel reflection coefficients is correct. One is now able to proceed with considerable confidence in separating the effects of large and small scale structures from each other.

An additional implication of the 2.2-m Brewster null is that there is no widespread, uniform layering of the uppermost portions of the surface greater than about 25 cm, and less than several meters. This is not in disagreement with the notion of a regolith underlain by a rough interface, or gradual transition to bedrock.

- (b) Reflectivity Differences between Highland and Maria. The observed greater quasi-specular reflectivity of the lunar maria with respect to lunar highlands is in opposition to the earth-based backscatter observations which show the highland areas to be brighter. The reason for this difference is not known, but it may be due to the marked smoothness of the maria with respect to the highlands, a greater depth of the lunar regolith in highlands with respect to maria, an intrinsic difference in the material of the highlands with respect to maria, or some combination of these effects. This measurement provides a severe constraint which future electromagnetic models of the lunar surface must satisfy.
- (c) Variations in Surface Reflectivity within Oceanus Procellarum. The high radar reflectivity anomalies within Oceanus Procellarum are associated with areas of the lunar surface which are believed, on the basis of crater morphology, to be quite young and thus possess only a thin regolithic layer. This association of thin regolith and high reflectivity suggest a model in which the forward scattered quasi-specular echoes are composed of two components, one from the upper visible surface and the second attenuated reflection from the interface of the regolith and the underlying bedrock. The depth of the regolith inferred from such a model and the electromagnetic parameters required of the surface material are completely consistent with laboratory measurements of similar materials and the depth of the regolith inferred from Lunar-Orbiter and Ranger photography in selected locations. We believe that this consistency argues very strongly for the adoption of a two-layer radar model of the lunar surface and for a re-interpretation of the ground-based radar observations in the light of a radar "translucent" regolith.
- (d) Lunar Surface Slopes. The bistatic-radar experiment has provided the first electromagnetic method for unambiguously separating the effects of lunar surface shape from those of surface

material. The (average) slopes obtained by this technique are considerably lower than those previously inferred from ground-based observations but do agree, at the limited number of places where cross checking is possible, with those obtained by photoclinometric techniques and photogrammetry. It has also been shown that there are considerable (3:1) topographic variations in the average lunar slopes and that previous assumptions regarding the homogeneity of the lunar surface for the purposes of radar analysis must be reconsidered.

Much more detailed accounts of the scientific results of this work and its implications are given in the three references listed at the beginning of this section.

PRECEDING PAGE BLANK NOT FILMED.

V. DATA ACQUISITION

Data for this experiment was collected in the six-month period following spacecraft launch using the Stanford Research Institute 150-ft dish antenna and in September 1968 using the Arecibo Ionospheric Observatory 1000-ft dish antenna. In all, approximately 150 hrs of data were collected. The Stanford receiving system hardware consists of a set of very narrow tracking filters which could be offset by variable amounts from the downlink telemetry carrier. Two separate but coherent receiving channels were employed, for both right and left circular polarization. The outputs of the receivers were recorded on magnetic tape for subsequent reduction and analysis. A similar system was employed at Arecibo but without the automatic frequency tracking feature.

An estimate of the frequency of the echo signal with respect to the downlink carrier is a prerequisite to data collection. These estimates were calculated at Stanford on the basis of orbital predictions supplied by the Goddard Space Flight Center. This technique was found to be quite reliable and accurate.

The receiving system hardware and the software for frequency prediction have been described in detail in previous reports and will not be reviewed here. The reader is referred to Tyler [1968c,d] for more information on this subject.

Observations were limited by the orbital geometry and the frequency spectrum of the downlink transmission. The geometric constraints were obvious. Since the spacecraft orbit is roughly equatorial, the loci of specular points on the lunar surface are also confined to that region. However, the orbital geometry also determines the frequency shift of the echo with respect to the directly propagating waves. Detection of the echo was possible only when this frequency shift caused the echo signal to fall between the downlink carrier and the adjacent modulation sidebands. This latter effect produced a noticeable thinning of the data corresponding to echoes from the central region of the lunar disk.

PRECEDING PAGE BLANK NOT FILMED.

VI. REDUCTION AND ANALYSIS OF ECHO DATA

A. Data Reduction

Data reduction of bistatic-radar echoes was employed on a two-step digital spectral analysis technique. First, the analog tapes were digitally sampled, blocks of the sample data trains sequentially converted to Fourier coefficients, and the Fourier coefficients written on magnetic tape. This process was carried out under the control of a single computer program. Second, the Fourier coefficients were combined to form spectral estimates under the control of an ancillary program which provided for on-line plotting and line printer output of the results. The bandwidths and integration times associated with the spectral analysis could be chosen and varied by the computer operator in this second step, thus providing a mechanism for adjusting the data reduction process in response to the changing character of the echo signal. The on-line plots were used to monitor the results of this process, and as the basic means of echo detection. Quantitative results were obtained from the line printer outputs. Coherence between data channels (one for each polarization) was maintained throughout all the sampling and computation steps. The algorithm and procedures used in the spectral analysis have been described elsewhere [Tyler, 1969].

B. Measurements of Surface Reflectivity

Measurements of surface reflectivity were obtained by correcting measurements of total reflected powers by the known geometrical factors, as described in Section II of this report. Total echo power was obtained from the area under the portion of the spectrum corresponding to the echo, but above the baseline established by the ambient system noise level. This area was then compared with the area contained under the noise baseline in a fixed bandwidth to obtain a measure proportional to absolute power which was independent of changes in receiver or processing gains.

Since the reflectivity of a dielectric is polarization dependent, knowledge of the incident and reflected polarization is an essential factor in the interpretation of the surface reflectivity. The results that have been published thus far are based upon observations where the incident

polarization was sufficiently simple so that it could be unambiguously determined by inspection of the spacecraft antenna patterns supplied by Goddard Space Flight Center. In attempting to use the antenna patterns where the polarization was more complex, it was discovered that the patterns must be in serious error. Eventually, it was possible to determine the source of error and make reasonable corrections to the patterns supplied, but only at the expense of considerable effort and time. A thorough discussion of the antenna pattern problem is given in the Appendix.

C. Measurement of Slopes

Measurements of lunar surface slopes are based on the spread, or frequency broadening of the echoes. Again, the quantity is obtained from the computed spectra, but is simply measured from the plots. The one-half power bandwidth is simply the width of the echo midway between its peak and the noise baseline. To the extent that the echoes represent true quasi-specular reflections this measurement is independent of polarization. There are no examples in the data of statistically significant differences between the values obtained in the two polarizations. The measured values are then corrected for variation in orbital attitude and velocity according to the theory given in Section II. Again, the final trajectories supplied by Goddard Space Flight Center are used. This work has been completed for all the data taken at Stanford.

VII. OCCULTATIONS

A second mode of experimentation is possible at the times when the satellite enters into, and emerges from, occultation by the moon. At those times, the signal from the satellite undergoes Fresnel diffraction by the lunar limb, and the signal received on the earth is characteristic not only of its source but also of the lunar surface in the neighborhood of the occultation.

There are two goals for analysis of occultations of a satellite by the lunar surface. First and simplest is to catalog the "Fresnel response" of the limb for all observable locations. Such a catalog could be useful to radio astronomers who [following Scheuer, 1962; Hazard, 1962] use lunar diffraction to resolve fine detail of radio-sources. That resolution process assumes the observed intensity during occultation to be a convolution of the actual radio brightness with the Fresnel diffraction of a point-source by an ideal edge. Using the satellite as a source, one could establish the exact empirical nature of the "edge" of the lunar limb, and thus offer a more accurate standard for deconvolution to diffraction astronomers.

An extension of the data analysis could yield actual surface information in the neighborhood of the occultations. Such an approach would view the limb as an aggregate of many diffracting edges at various ranges and heights. The analysis proceeds along much the same lines as Scheuer has described. The difference is that his case of a compound source and a simple edge causes a superposition of diffraction curves whose periods are all identical. The situation of a point source and a complex edge leads to various periods as well, because features to one side of the occultation line cut through the Fresnel zones at an angle. Thus from each occultation one can extract information about the terrain of the limb in that neighborhood.

Both applications of occultation measurements--an empirical cataloging and surface mapping--depend crucially on deciphering the characteristics of the lunar limb from those of the source, Explorer 35. The data reduction problem is complicated by two effects inherent in the design of Explorer 35 and one due to the signal propagation path. The latter is a

random fluctuation in signal strength, for which no attempt at removal was made. The two sources of variation in the spacecraft source are modulation imperfections and antenna spin. If the carrier power should vary with modulation content, then the problem of normalizing the effect is very great, and that refinement was not attempted in this experiment. Correction for antenna patterns was made, and that constitutes about half of the data reduction problem.

The occultation experiment yielded several processed diffraction patterns. Of these, the most usable still exhibits significant nondiffraction perturbations. These perturbations may well be vestigial antenna pattern variations, but the possibility of carrier power variations with modulation frequency must also be considered. The methods used to refine the data as well as proposed improvements are dealt with in subsequent sections of this report.

A. Occultations: Data Acquisition

All occultations used to obtain diffraction patterns were immersion (entering occultation) cases, so that the receiver was locked on the satellite signal through essentially the entire diffraction pattern. The first three occultations processed were taken from tapes recorded with Stanford's 150-ft dish, which has been described above. In order to obtain more recordings, a receiving station was later assembled around a 30-ft dish not currently in use at Stanford. With a circularly polarized feed, signal strength was adequate for receiver lock-on. An instrumentation recorded taped in-phase and quadrature components of the carrier as well as a 1000-Hz clock, WWV, and the telemetry signal demodulated. The tapes were then played back and digitized using the Center's Sigma 5 computer. The simple data-gathering arrangement allowed the recording of many occultations of which the three best were chosen to be further processed and analyzed, as had those obtained from the 150-ft dish installation.

B. Occultations: Data Reduction

The first attempt to process Explorer occultations at the Center drew on existing tapes recorded with Stanford's 150-ft antenna. Of these, three contained occultation immersions and those were examined. The emersions recorded were not usable due to lack of receiver lock on the satellite carrier signal. Of the three tapes chosen, one was significantly better than the other two, one of which had data dropouts and the other had the carrier nearly out of range of the low-pass filter used. The best tape, recorded 9 November 1967, supplied data for our first attempts at processing. Figure 4 depicts the sequence described below.

Step 1: Sampling. The carrier signal recorded had been heterodyned to roughly 200 Hz. Using a synchronous clock pulse on the data tape, samples were taken and digitized at a rate of 512/sec. Each sample was complex-valued, thus preserving all frequencies from -256 Hz to +256 Hz.

Step 2: Fourier Analysis. Of the data sampled, the 64 seconds including the occultation immersion were read from tape into core memory at Stanford's IBM 360/67 installation. At this point, all 32,768 complex samples were transformed into the frequency domain using our version of the Cooley-Tukey Fast Fourier Transform. A transform of such size furnishes a resolution of 0.008 Hz for further data manipulation.

Step 3: Digital Heterodyning to DC. With the data spectrum in storage, the processing program scans the spectrum for the highest spectral peak outside the neighborhood of DC. This peak is the carrier. Erroneous choices would be detected, since the value chosen is printed out, and can be visually checked for correspondence to the peak in the spectrum, which is plotted on a Calcomp plotter attached to the computer. When the carrier has been located, the spectrum is simply shifted in place so that the carrier peak is moved to DC exactly.

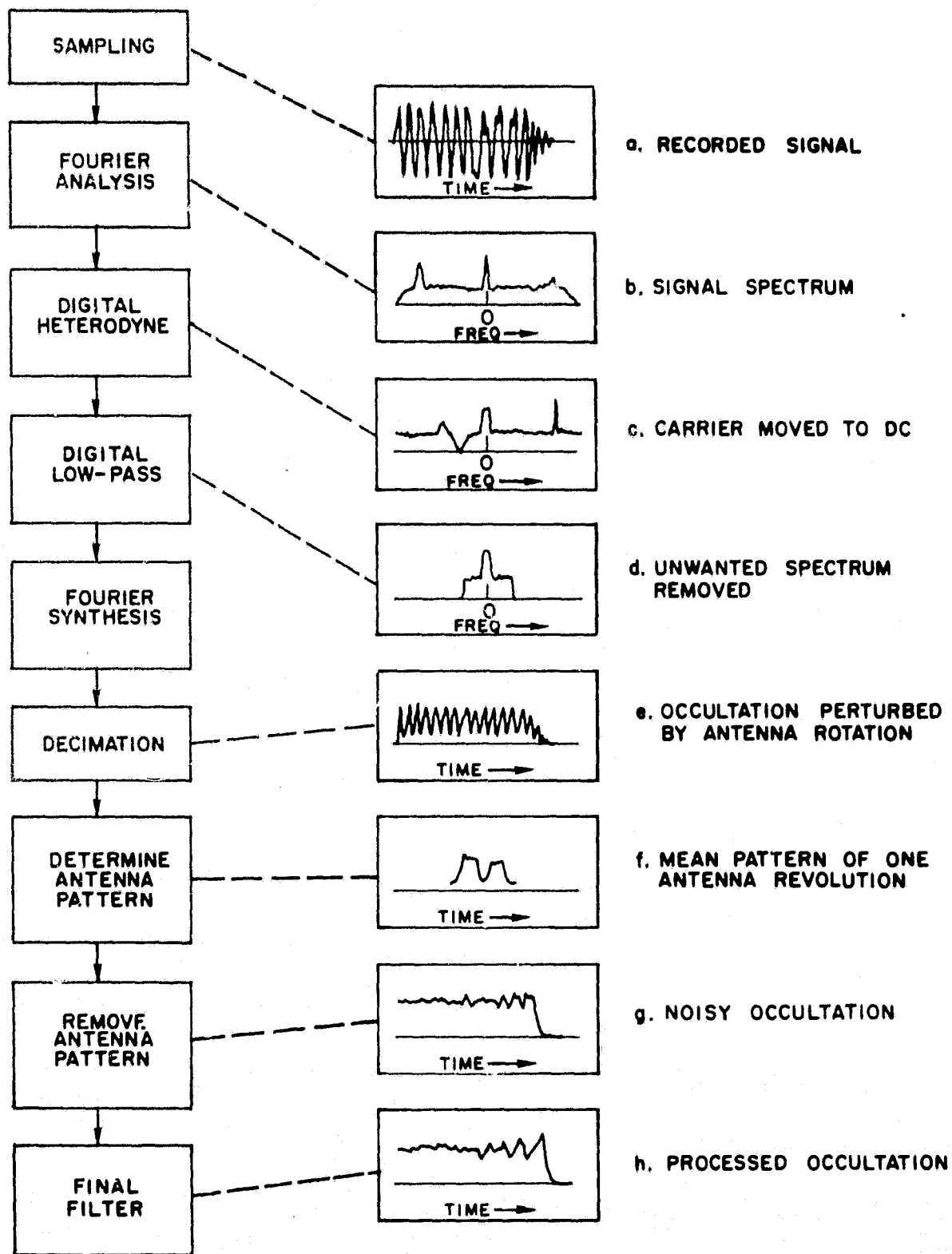
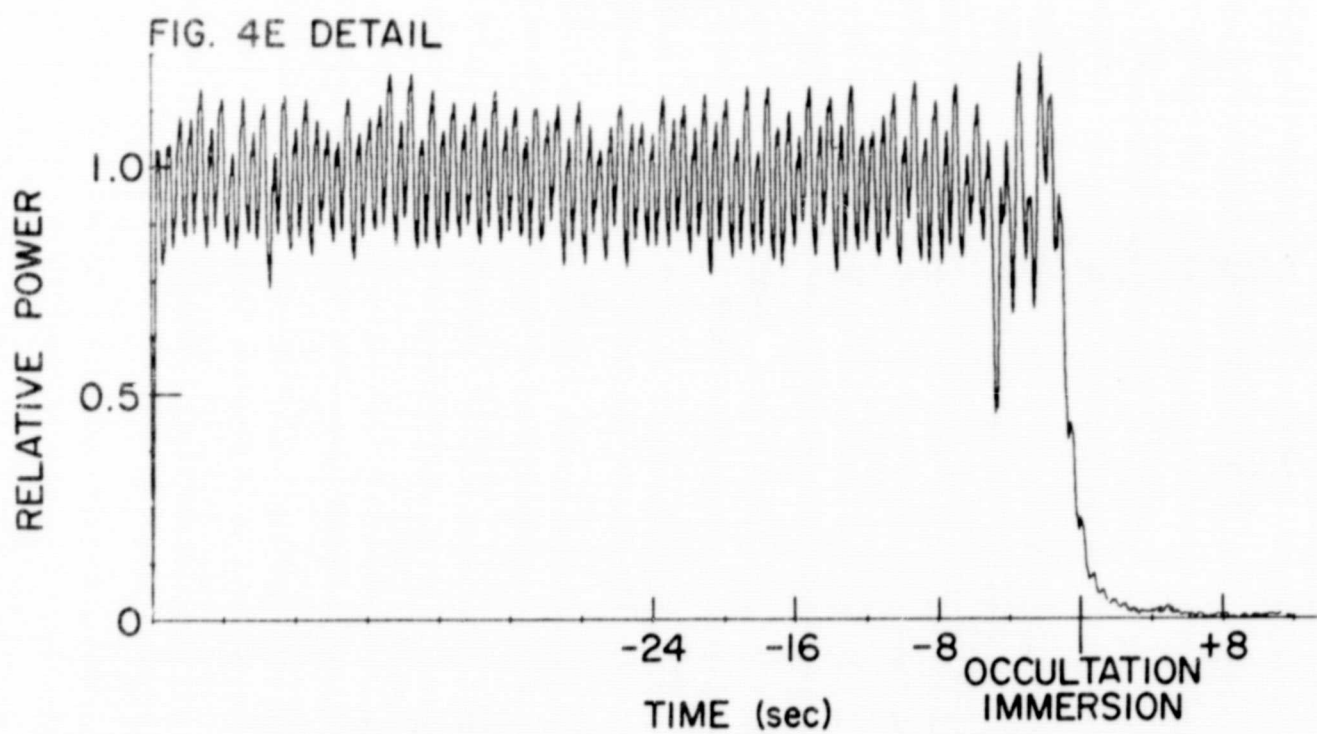
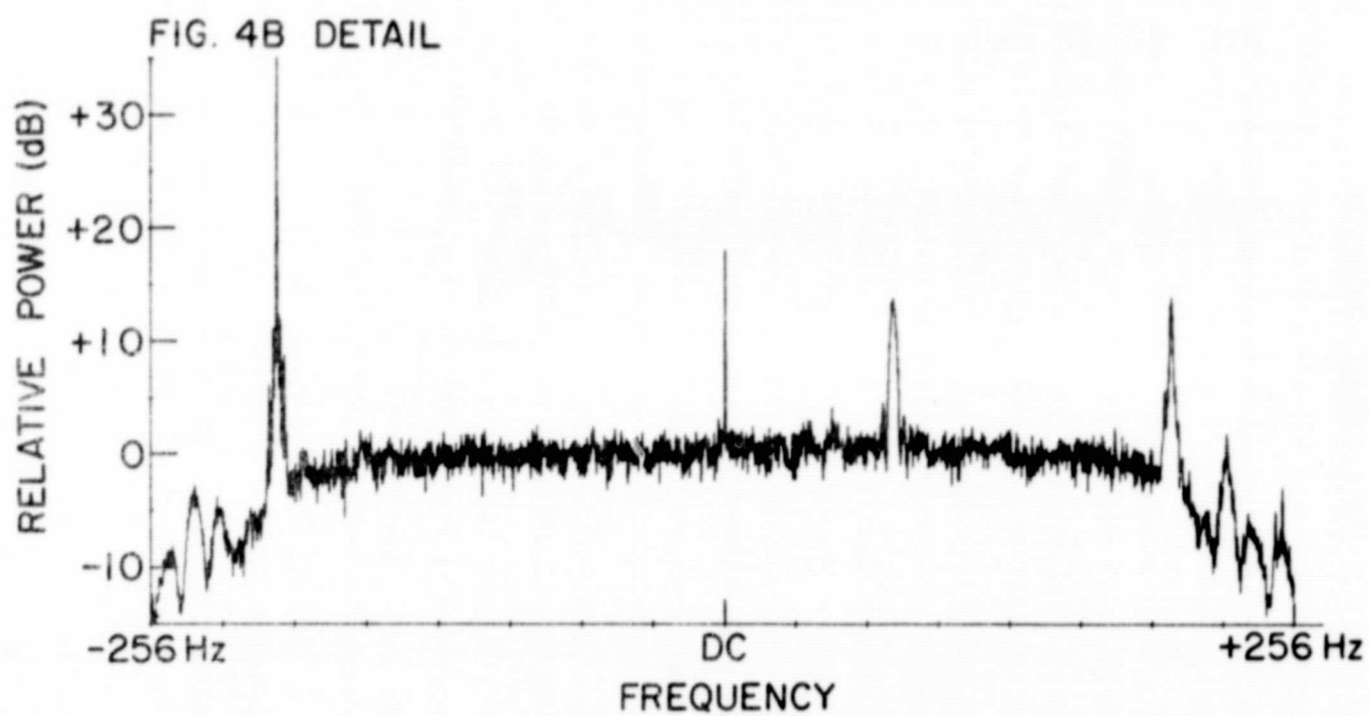


Fig. 4. OUTLINE OF DATA PROCESSING FOR OCCULTATION OBSERVATIONS.



DETAILED DRAWING OF FIG. 4b "SIGNAL SPECTRUM" AND FIG. 4e "OCCULTATION PERTURBED BY ANTENNA ROTATION."

FIG. 4G DETAIL

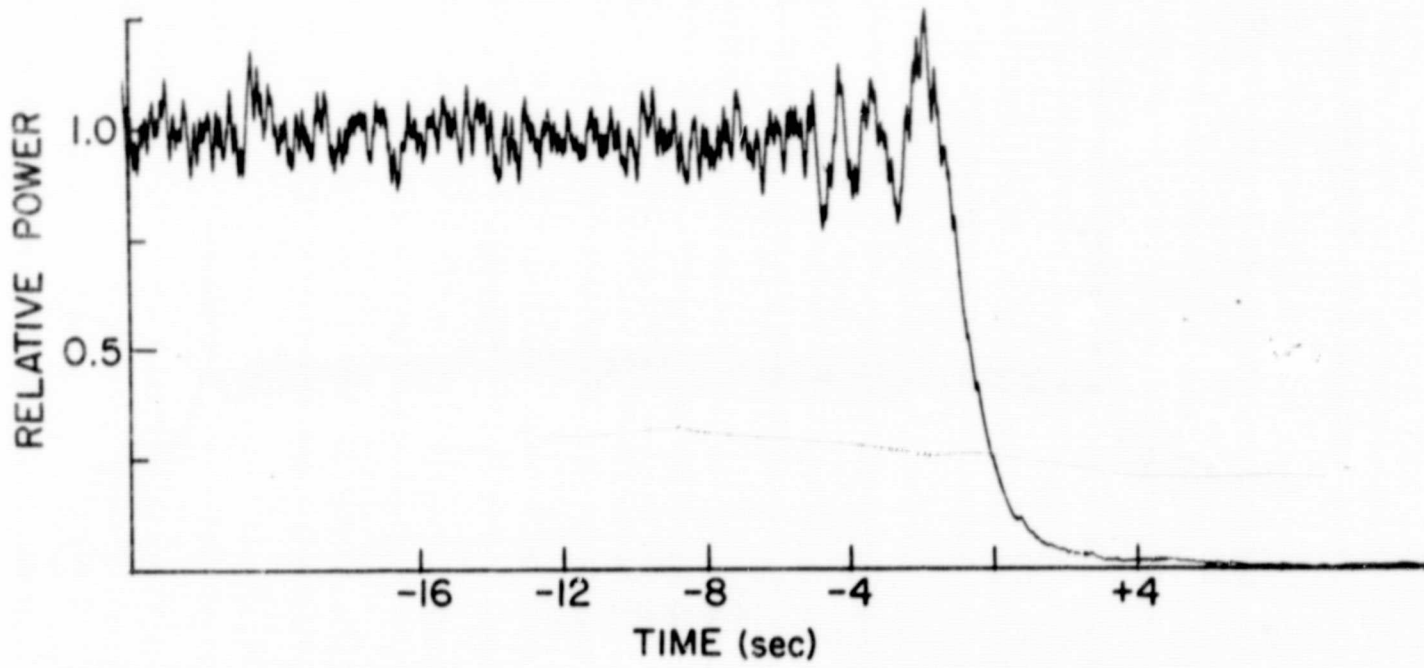
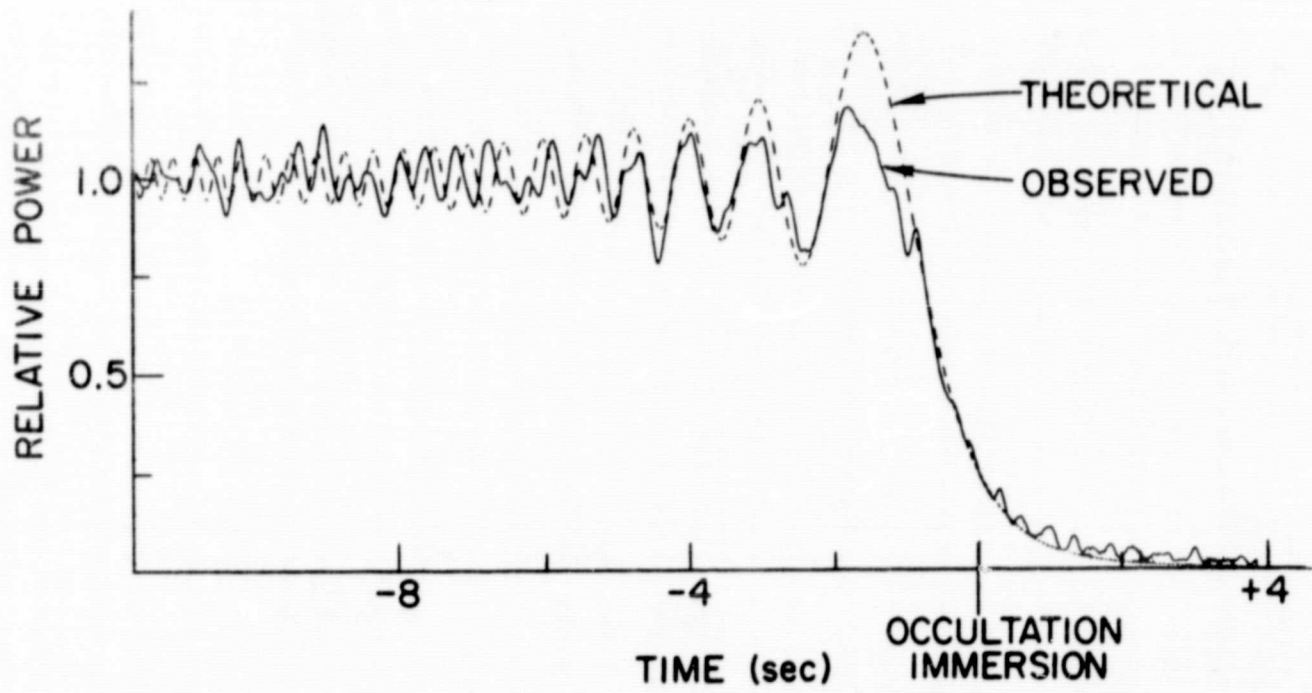


FIG. 4H DETAIL



DETAILED DRAWING OF FIG. 4g "NOISY OCCULTATION" AND FIG. 4h "PROCESSED OCCULTATION."

Step 4: Digital Low-Pass Filtering. The translated spectrum is now multiplied by a "window" 32 Hz wide centered at DC. The "window" used had edges shaped to $\sin^2(x)$ and gave a very good step-response to the filter. The spectrum now contains only the carrier (translated to DC) and related components within a 16-Hz neighborhood. Most noise is thus eliminated, especially since only the useful side of the spectrum (original signals were complex) is retained.

Step 5: Fourier Synthesis. The heterodyned and windowed spectrum is now retransformed to yield a filtered version of the occultation.

Step 6: Decimation. Since the processed version is now limited to frequency components below 16 Hz, it may be sparsely sampled at 32 Hz, thus decimating the original 32,768 samples to 2,048 complex samples. These samples are punched onto data cards for preservation. Inspection of the data at this point reveals a signal which dies away at the time of occultation, but no features can be seen other than the overwhelming variations from the rotation of Explorer 35's antenna.

Step 7: Determination of Antenna Pattern. The crucial stage in processing occultations of Explorer 35 is that of removing the antenna rotation modulation. The antenna variation can be much stronger than the greatest variation in the Fresnel diffraction. Because the period is comparable to the main Fresnel diffraction period, spectral separation is difficult; the more so owing to the harmonic content of the antenna pattern. Our method first determines the antenna pattern in the time domain, then divides the data by that pattern to normalize the unwanted modulation.

Starting with an estimate of the antenna period, the computer averages every repetition of that period to obtain a mean antenna pattern shape. Neither noise nor the Fresnel pattern are selected by this period averaging. The process is repeated for many values of period in the neighborhood of the original estimate, and from these

the best antenna pattern is chosen according to a least-mean-square-error criterion.

Step 8: Removal of Antenna Pattern. The best version of one antenna revolution is repeated to generate an ideal antenna pattern. Then the entire occultation waveform is divided by that ideal antenna pattern to remove the undesired variations.

Step 9: Final Filtering. The final processing of the occultation consists of a derivative clamp to remove noise spikes and a low-pass filter to smooth the final image for plotting.

C. Occultations: Analysis

Figure 4h depicts the finally processed occultation from 9 November 1967 along with a best-fit knife-edge Fresnel diffraction curve. Several features are worthy of note. First, there are definite Fresnel diffraction fringes on the processed signal, and the drop-off to zero signal follows the theoretical pattern well. Second, the extent of the diffraction lobes of the processed curve is less than that of the theoretical curve. If meaningful, this effect can be attributed to roughness of the lunar limb which smears the diffraction.

A third feature of note in Fig. 4h is not a desirable one--namely the large amount of noise in spite of elaborate processing. That many of the perturbations are not due to diffraction of the limb is shown by their curvature. Surface features could only effect a smooth smearing by superposing diffraction patterns of slightly different times and periods. The rate of change is fixed by the rate at which alternate phase zones from the satellite to the earth are crossed. Thus, in the summer of 1968, one good occultation had been obtained, but it was not good enough for fruitful analysis.

One obvious route out of this dilemma lay in recording more occultations. We were able to borrow a 30-ft dish for this purpose and it was set up to record Explorer 35 specifically at times of occultation immersion. The tapes recorded at that later time were even worse in their

undesired fluctuations. The smaller antenna seems not to have been the problem as receiver lock was good, and the carrier frequency structure was clearly evident in the spectra. We are left with only one further explanation for the spurious variations in signal observed--a possibility suggested by visually monitoring the carrier power while listening to the telemetry modulation from the satellite. Whatever the cause, the carrier power seems to vary with telemetry frequency. Ideal 1-rad square-wave phase modulation maintains a constant 30 percent of transmitted power in the carrier, the other 70 percent lying in the sidebands. Were the modulation (for the square-waves) not ideal, then resulting amplitude modulation of the carrier would explain the difficulties we have observed in extracting Fresnel diffraction from variations in the carrier power received. Moreover, a deterioration of the modulation with time would explain our difficulty in reproducing the partial success of our earlier processing efforts.

We believe we have solved the problems associated with removing enough spurious effects (noise and antenna modulation mostly) to observe empirical lunar diffraction. To further attempt correction of nonideal telemetry modulation seems more complicated than is reasonable to obtain diffraction information. Future occultation experiments will, as did this attempt, depend on a constant carrier signal. The surest guarantee is cessation of telemetry at immersion and emersion, but proper attention to the modular design should suffice. Much processing (and associated inaccuracy) would also be bypassed by choosing a rate of antenna gain variation either much slower or much faster than the approximate diffraction variation rate. Attention to the above considerations, coupled with such processing measures as we have employed, should yield the occultation data which we had hoped to extract from recordings of Explorer 35.

PRECEDING PAGE BLANK NOT FILMED.

VIII. CONCLUSIONS

This report concludes the data acquisition reduction and preliminary analysis phase of this work. A great deal more remains to be done in the realm of further analysis and interpretation. This work is continuing with additional support from NASA.

As we have pointed out here, the principal constraints on observations of this work are those of the orbital parameters and of the orbital parameters in combination with the design of the downlink telemetry spectrum. We would urge that, if experiments of this kind are conducted in the future, the orbits be highly inclined with respect to the equator of the central planet and that there be a consideration of the scientific implications of engineering decisions in the design of the telemetry subsystems.

... HOLDING PAGE BLANK NOT FILMED.

APPENDIX

To accurately describe the reflection process at a surface, it is necessary to know the polarization of both the incident and reflected waves. In the Explorer 35 experiment, left and right circular components were received and recorded on the earth, allowing determination of the polarization of the reflected wave, except for an unknown Faraday rotation. The purpose of this appendix is to describe the determination of the incident polarization from the satellite antenna patterns furnished by Goddard Space Flight Center (GSFC). Such patterns, in both linear and circular polarizations, generally provide accurate amplitude information but have ambiguities regarding phase which make it difficult to reconstruct actual radiated fields.

It was originally thought that computer synthesis of a mathematical model of the antenna would provide sufficient phase information to remove these ambiguities and allow a unique reconstruction of the radiated field from the patterns. However, in attempting to carry out this process it was discovered that the patterns supplied by GSFC must contain serious errors, since calculation of the total power radiated in a given direction, based on the linear and circular patterns, were inconsistent. Because of this difficulty it was necessary to rely heavily upon the model patterns. Eventually it was discovered that the discrepancies in the patterns could all be accounted for by a rotational misalignment of coordinates, and this is now believed to be the source of the difficulty.

1. Development of an Antenna Model

The procedure for modeling of the spacecraft antenna was straightforward; a brief description follows. The physical dimensions and arrangement of the spacecraft elements are shown in Figs. 5 and 6. To begin with one can consider the far field of a small dipole, which Kraus [1950] gives as

$$E_{\theta} = \frac{j60\pi [I]}{r} \sin \theta \frac{L}{\lambda} \quad (\text{A.1})$$

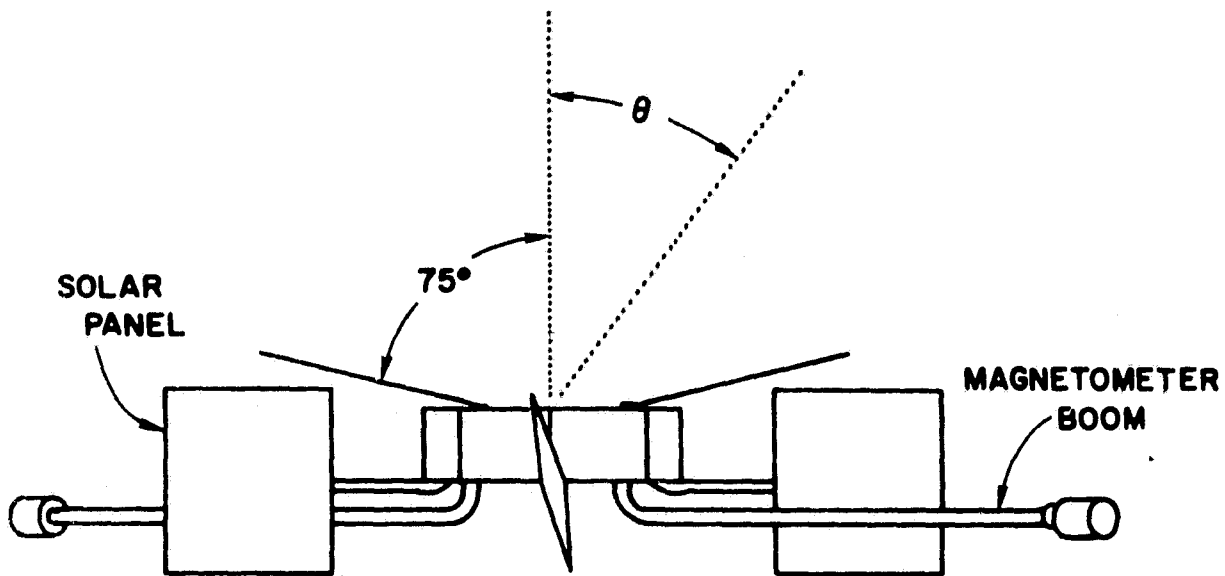


Fig. 5. SIDE VIEW OF THE EXPLORER 35 SPACECRAFT (NOT TO SCALE) SHOWING MEASUREMENT OF THE POLAR ANGLE θ .

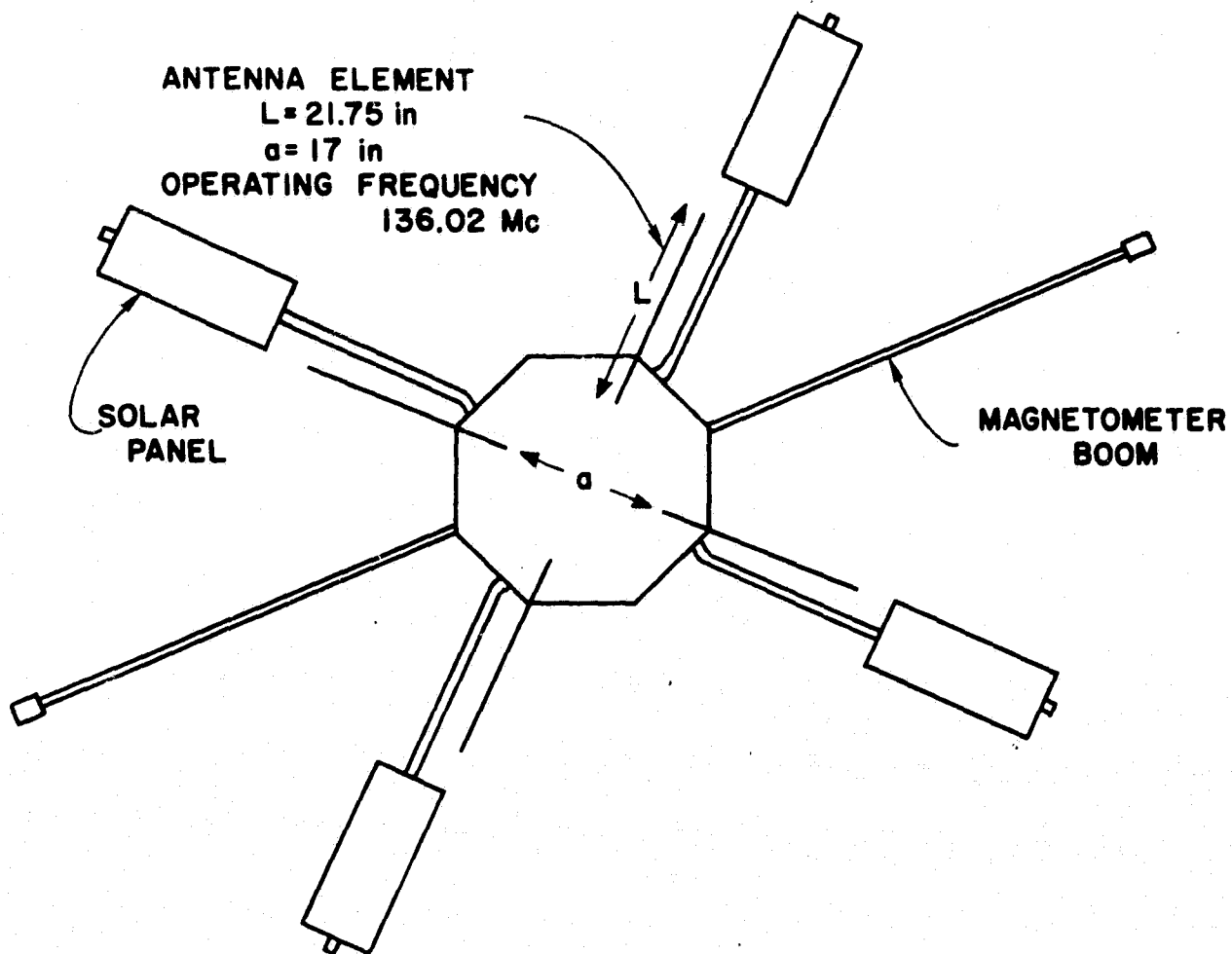


Fig. 6. TOP VIEW OF THE EXPLORER 35 SPACECRAFT (NOT TO SCALE). Angle of rotation ϕ , also called the azimuthal angle, is measured clockwise.

$$H_{\theta} = \frac{j[I]}{2r} \sin \theta \frac{L}{\lambda} \quad (\text{A.2})$$

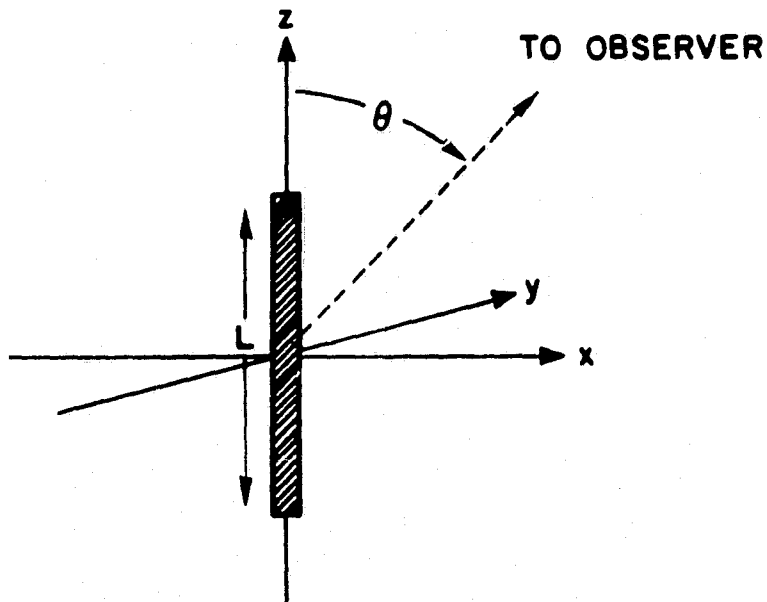
where $r' = r_0 - z' \cos \theta$

r_0 = distance to observer

θ = angle between the current element and the vector to the observer.

Such a dipole is oriented as shown in Fig. 7 and has uniform current distribution $I = E_0 \exp(j\omega t)$. I stands for the retarded field, $I_0 \exp[j\omega(t-r/c)]$.

Fig. 7. ORIENTATION OF A SMALL CURRENT ELEMENT IN xyz SPACE.



One can consider a current rod of arbitrary length to be made up of such infinitesimal dipoles (see Fig. 8). The length dz' at z' contributes

$$dE_{\theta} = \frac{j60\pi I(z')}{r} \sin \theta \frac{dz'}{\lambda} \exp[j\omega(t-r'/c)] \quad (\text{A.3})$$

to the overall field.

The total field is the integral of (A.3) or

$$E_{\theta} = \frac{j60\pi}{r\lambda} \sin \theta \exp(j\omega t - j\beta r_0) \int_{-d/2}^{d/2} I(z') \exp(j\beta z' \cos \theta) dz' \quad (\text{A.4})$$

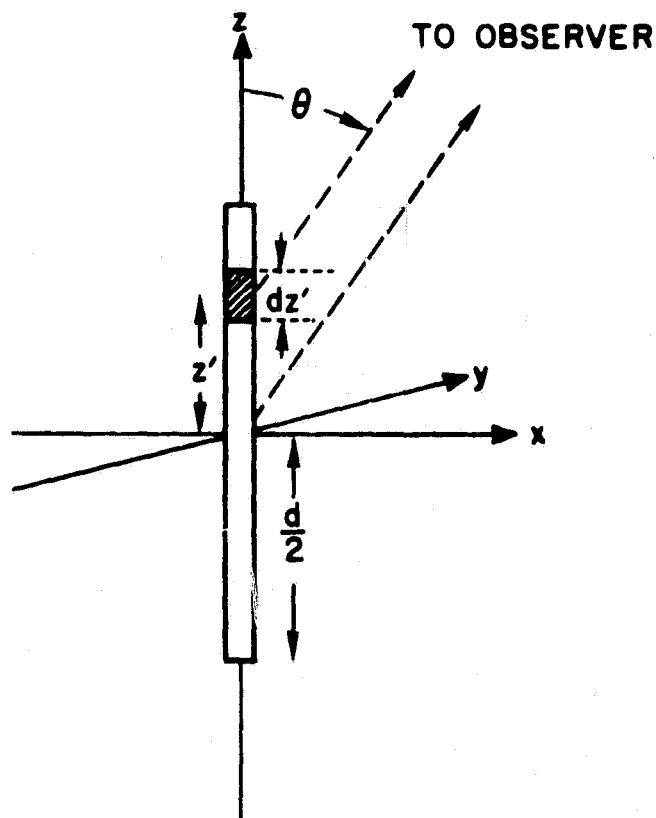


Fig. 8. A CURRENT ROD OF ARBITRARY LENGTH d CAN BE APPROXIMATED BY A SUM OF SMALLER CURRENT ELEMENTS.

The entire current rod is defined to be oriented in the $+\bar{a}_z$ direction. The boundary condition $I(z = d/2) = 0$ is applied at one end, but the other will be allowed to have any finite value of I .

If a sinusoidal current is assumed, distribution along the rod is

$$I(z') = I_0 \cos \left(\frac{z'}{d} + \frac{1}{2} \right) \frac{\pi}{2} = I_0 \cos \left(\frac{\pi}{4} + \frac{\pi z'}{2d} \right) \quad (\text{A.5})$$

so that

$$E_{\theta} \propto \sin \theta \exp(-j\beta r_0) \int_{-d/2}^{d/2} \left\{ \exp \left[j \left(\frac{\pi}{4} + \frac{\pi z'}{2d} \right) \right] + \exp \left[-j \left(\frac{\pi}{4} + \frac{\pi z'}{2d} \right) \right] \right\} \exp(j\beta z' \cos \theta) dz'$$

(A.6)

$$= \sin \theta \exp(-j\beta r_0) \exp[j(\pi/4)] \int_{-d/2}^{d/2} \exp\left[j\left(\frac{\pi}{2d} + \beta \cos \theta\right) z'\right] dz' \quad (\text{A.7})$$

$$+ \sin \theta \exp(-j\beta r_0) \exp[-j(\pi/4)] \int_{-d/2}^{d/2} \exp\left[-j\left(\frac{\pi}{2d} - \beta \sin \theta\right) z'\right] dz'$$

$$= \sin \theta \exp(-j\beta r_0) 2j \frac{\exp[j(\pi/4)] \sin\left(\frac{\pi}{2d} + \beta \cos \theta\right) \frac{d}{2}}{j\left(\frac{\pi}{2d} + \beta \cos \theta\right)} \quad (\text{A.8})$$

$$+ \sin \theta \exp(-j\beta r_0) (-2j) \frac{\exp[-j(\pi/4)] \sin\left(\frac{\pi}{2d} - \beta \sin \theta\right) \frac{d}{2}}{-j\left(\frac{\pi}{2d} - \beta \sin \theta\right)}$$

$$= \frac{d}{\sqrt{2}} \sin \theta \exp(-j\beta r_0) \left[\frac{(1+j) \sin\left(\frac{\pi}{4} + \frac{\beta d}{2} \cos \theta\right)}{\left(\frac{\pi}{4} + \frac{\beta d}{2} \cos \theta\right)} + \frac{(1-j) \sin\left(\frac{\pi}{4} - \frac{\beta d}{2} \cos \theta\right)}{\left(\frac{\pi}{4} - \frac{\beta d}{2} \cos \theta\right)} \right] \quad (\text{A.9})$$

Rather than carry along a large number of similar terms, it is convenient to let RE and IE be the real and imaginary parts of E_θ where

$$\text{RE} \propto \sin \theta \left[\frac{\sin\left(\frac{\pi}{4} + \frac{\beta d}{2} \cos \theta\right)}{\left(\frac{\pi}{4} + \frac{\beta d}{2} \cos \theta\right)} + \frac{\sin\left(\frac{\pi}{4} - \frac{\beta d}{2} \cos \theta\right)}{\left(\frac{\pi}{4} - \frac{\beta d}{2} \cos \theta\right)} \right] \quad (\text{A.10})$$

and

$$\text{IE} \propto \sin \theta \left[\frac{\sin\left(\frac{\pi}{4} + \frac{\beta d}{2} \cos \theta\right)}{\left(\frac{\pi}{4} + \frac{\beta d}{2} \cos \theta\right)} - \frac{\sin\left(\frac{\pi}{4} - \frac{\beta d}{2} \cos \theta\right)}{\left(\frac{\pi}{4} - \frac{\beta d}{2} \cos \theta\right)} \right] \quad (\text{A.11})$$

The proportionality factors are equal and $\exp(-j\beta r_0)$ has been purposely omitted (it will appear in the array factor later).

If an array is formed from a number of these current rods, the total field is the sum of the individual fields. The individual elements are assumed to be oriented in the directions $\bar{a}_{z_1}, \bar{a}_{z_2}, \dots, \bar{a}_{z_n}$; the vector distances and directions of the midpoint of each rod from the center of the array are given by $\bar{\rho}_1, \bar{\rho}_2, \dots, \bar{\rho}_n$. The unit vector from the origin (center of the array) to the observer is \bar{i}_r which makes an angle θ_i with each \bar{a}_{z_i} .

The vector \bar{a}_{z_i} will have components a_{i1}, a_{i2}, a_{i3} in the coordinate system of the array. The vector \bar{i}_r can also be described in this same coordinate frame. Together \bar{a}_{z_i} and \bar{i}_r determine a plane--the same plane in which \bar{E}_{θ_i} lies. It follows that \bar{E}_{θ_i} may be decomposed into two components--one parallel to \bar{a}_{z_i} and a second perpendicular to \bar{a}_{z_i} .

The following definitions can be made (see Fig. 9):

$$\bar{i}_r \times \bar{a}_{z_i} \triangleq \bar{c}_i \quad (\text{A.12})$$

$$\bar{c}_i \times \bar{a}_{z_i} \triangleq \bar{n}_i \quad (\text{A.13})$$

Then $\bar{n}_i / |\bar{n}_i|$ is the unit vector perpendicular to \bar{a}_{z_i} and \bar{E}_{θ_i} can be expressed as a linear combination of \bar{n}_i and \bar{a}_{z_i} .

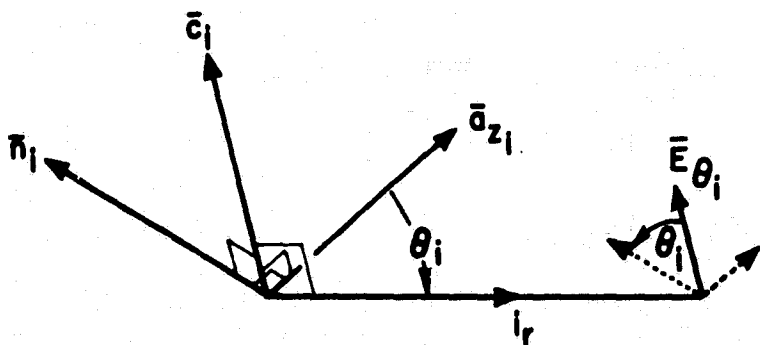


Fig. 9. AN OBSERVER WILL DETECT AN ELECTRIC FIELD \bar{E}_{θ_i} FROM A CURRENT ELEMENT. \bar{E}_{θ_i} will have components in the direction of the element (\bar{a}_{z_i}) and perpendicular to it (\bar{n}_i).

For each current element there will be a pair of parallel and perpendicular unit vectors. One can designate $\bar{u}_{\parallel i}$ as the set of all parallel vectors and $\bar{u}_{\perp i}$ the set of all perpendicular vectors. Multiplying each $\bar{u}_{\parallel i}$ by the corresponding $\sin \theta_i$ and each $\bar{u}_{\perp i}$ by $\cos \theta_i$ gives the proportional E_{θ_i} in each direction. The sum $\bar{u}_{\parallel i} \sin \theta_i + \bar{u}_{\perp i} \cos \theta_i$ gives a single vector in xyz space which, when multiplied by the magnitude of E_{θ_i} (i.e., $RE_i + jIE_i$), gives the field at the observer due to current element i .

Because each element is displaced from the origin by $\bar{\rho}_i$ there will be an array factor. Each element will have a phase factor

$$\exp[j\beta(\bar{i}_r \cdot \bar{\rho}_i)] = \cos \beta(\bar{i}_r \cdot \bar{\rho}_i) + j \sin \beta(\bar{i}_r \cdot \bar{\rho}_i) \quad (\text{A.14})$$

The total field at the observer will be the sum

$$\bar{E} = \sum_{i=1}^n [\cos \beta(\bar{i}_r \cdot \bar{\rho}_i) + j \sin \beta(\bar{i}_r \cdot \bar{\rho}_i)] [RE_i + jIE_i] \bar{u}_i \quad (\text{A.15})$$

where \bar{u}_i is the unit vector in the direction of \bar{E}_{θ_i}

$$\bar{u}_i = \bar{u}_{\parallel i} \sin \theta_i + \bar{u}_{\perp i} \cos \theta_i \quad (\text{A.16})$$

If each element were driven with a different phase, there would be an additional factor of $\exp(j\delta_i)$ included in (A.14) as

$$\exp[j\beta(\bar{i}_r \cdot \bar{\rho}_i)] \exp(j\delta_i) = \cos(\beta\bar{i}_r \cdot \bar{\rho}_i + \delta_i) + j \sin(\beta\bar{i}_r \cdot \bar{\rho}_i + \delta_i) \quad (\text{A.17})$$

Equation (A.15) would then have been

$$\bar{E} = \sum_{i=1}^n [\cos(\beta \bar{i}_r \cdot \bar{\rho}_i + \delta_i) + j \sin(\beta \bar{i}_r \cdot \bar{\rho}_i + \delta_i)] [R E_i + j I E_i] \bar{u}_i \quad (\text{A.18})$$

A program written for $n = 4$ was tested for a number of simple rod orientations such as the half-wave dipole, full-wave dipole, four-element broadside array, four-element end fire array, and turnstile. The patterns obtained were sufficiently close to be convincing.

The model of the Explorer 35 antenna was synthesized using the dimensions and arrangement of elements shown in Figs. 5 and 6; henceforth this will be referred to as the "ideal model" to distinguish it from various scaled models introduced later. Typical linear and circular patterns for the ideal model are shown in Figs. 10 and 11. These can be compared with the corresponding measured patterns in Figs. 12 and 13.

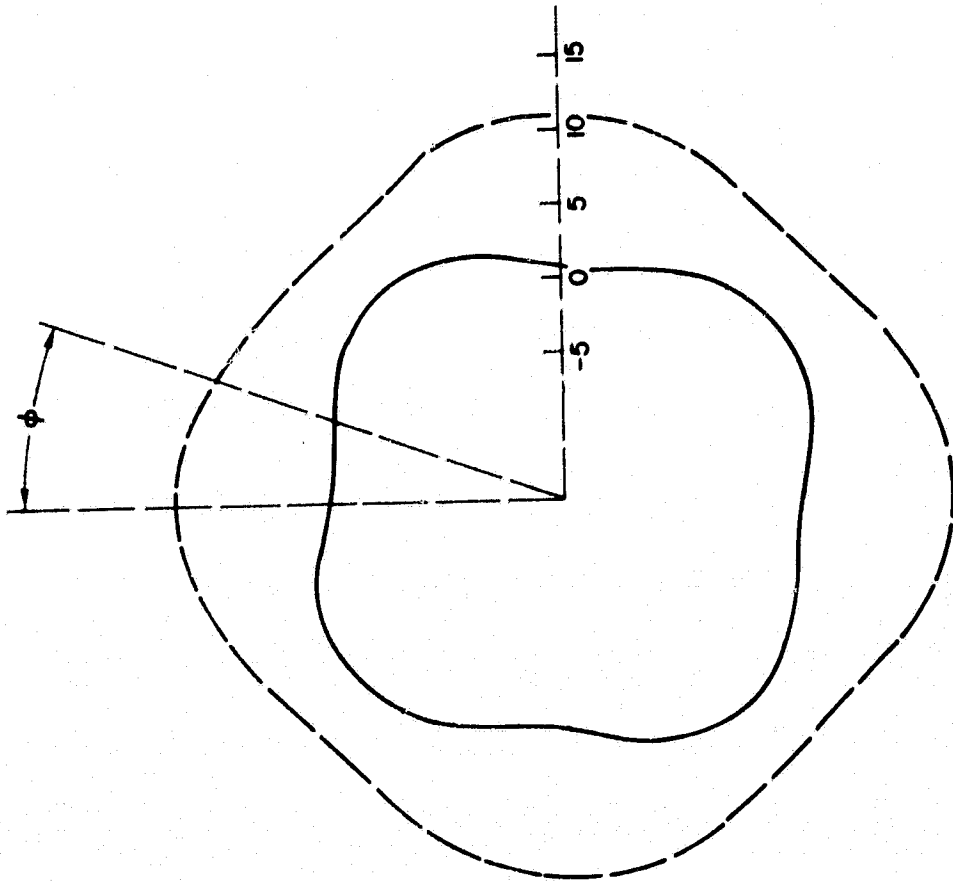
2. Comparison of the Model with Measured Patterns, Scale Factors

Antenna patterns supplied by GSFC are given in 15-degree (Figs. 12 and 13 being two representative cases) increments of the polar angle θ . A set of linear (or circular) patterns consists of the measured power in E_θ and E_ϕ (or E_L and E_R) components over a 360° rotation at a fixed polar angle. The Explorer 35 antenna is a modified turnstile, or a pair of crossed dipoles, and the radiation patterns range from nearly perfect left circular polarization at $\theta = 0$ (top view) to nearly perfect right circular polarization at $\theta = 180^\circ$ (bottom view).

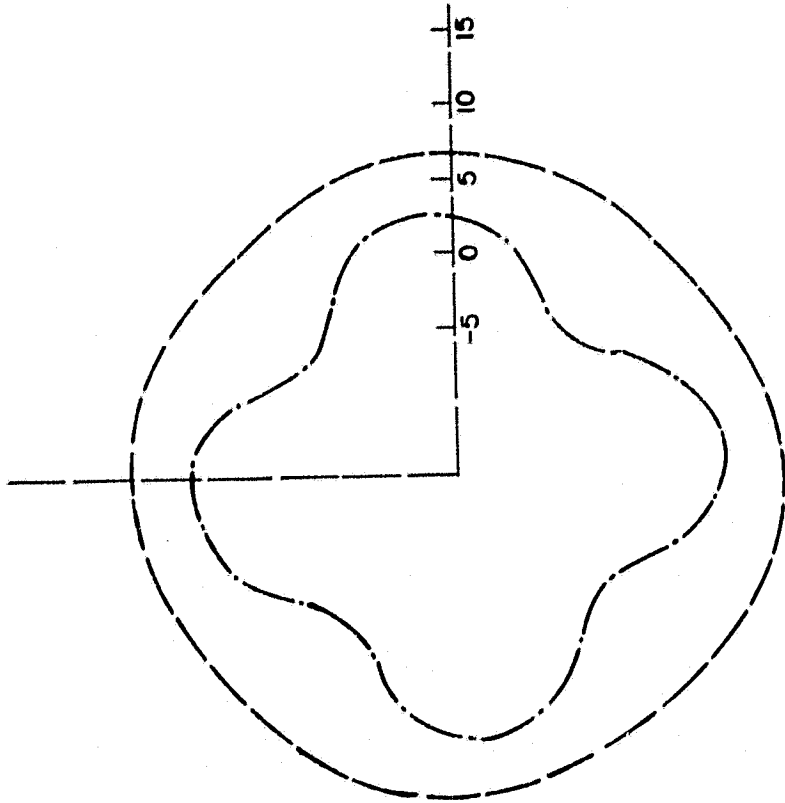
All antenna elements are tilted upward slightly at about 15° resulting in a top-to-bottom gain of about 3 dB. The presence of solar panels and magnetometer booms as well as the body of the spacecraft appears to have caused some distortion of the fields which is especially noticeable in the $\theta = 105^\circ$ and $\theta = 120^\circ$ patterns.

Although the distortion caused the pattern shapes to be modified, the main effect was to change the amplitude of the signal radiated. To account for the variation of amplitude with θ it was decided to find a polynomial scaling function of the form

$$f(\theta) = C_4 \theta^4 + C_3 \theta^3 + C_2 \theta^2 + C_1 \theta + C_0 \quad (\text{A.19})$$

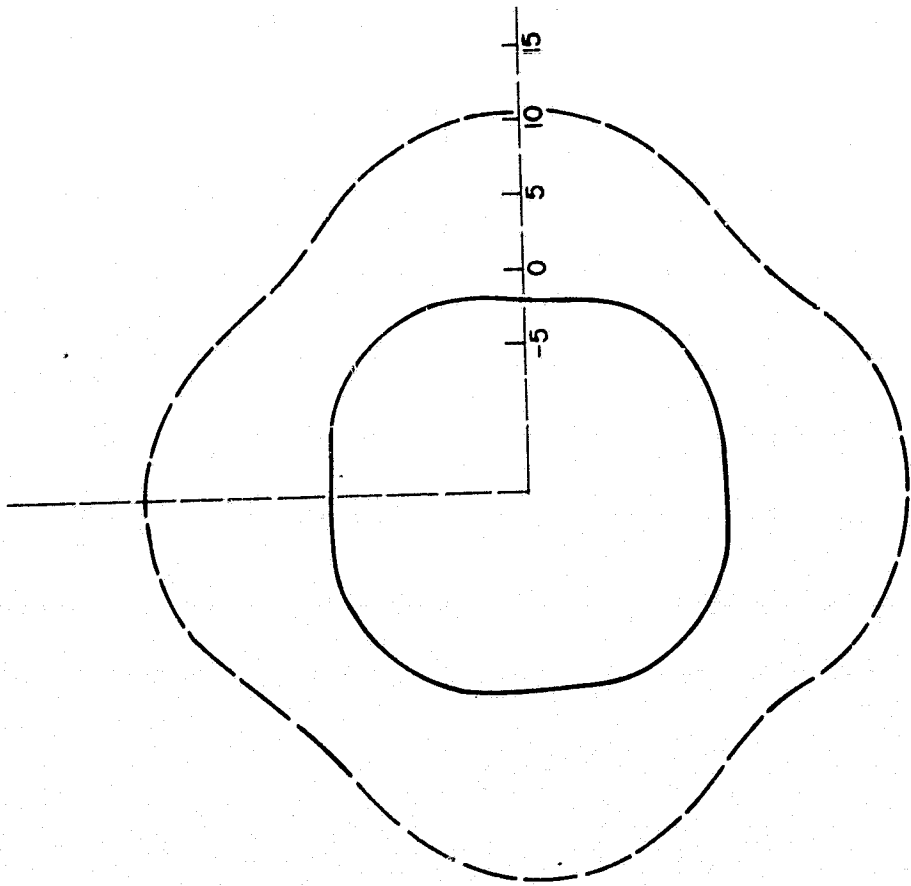


a. Linear

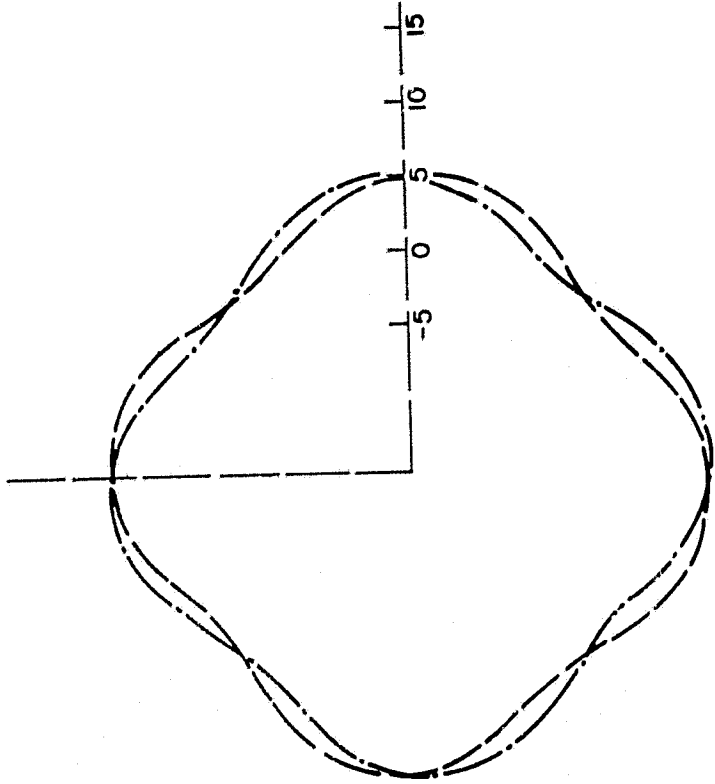


b. Circular

Fig. 10. LINEAR AND CIRCULAR RADIATION PATTERNS OF THE IDEAL ANTENNA MODEL AT A POLAR ANGLE OF $\theta = 60^\circ$. (scale is in decibels). a. Solid line is E_θ , dashed line is E_ϕ ; b. Dashed line is left circular, dashed dot line is right circular.

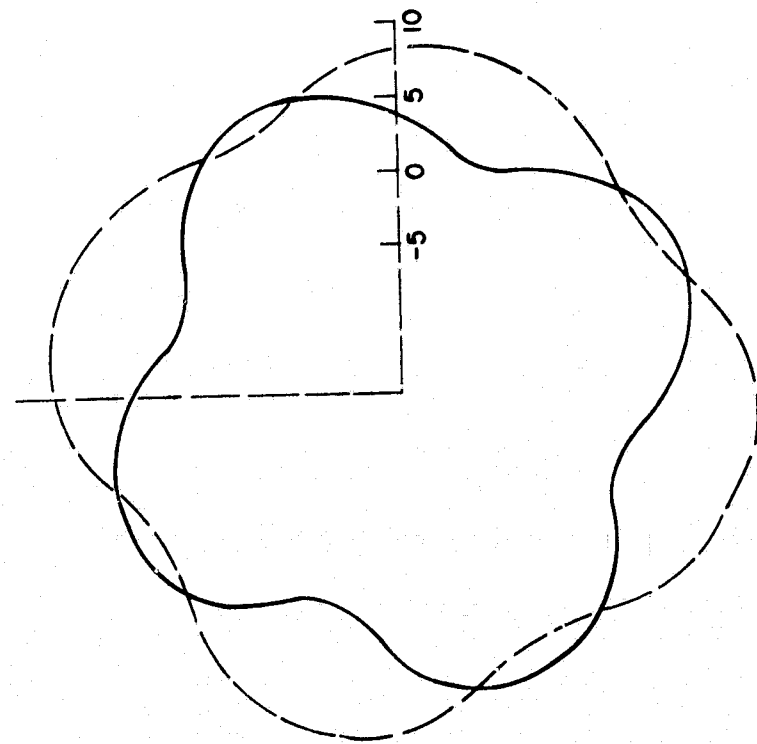


a. Linear

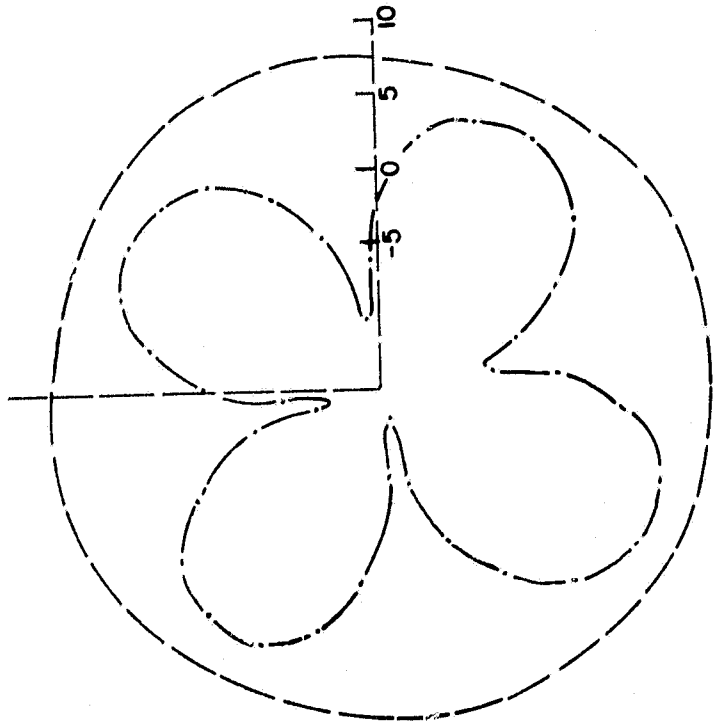


b. Circular

FIG. 11. LINEAR AND CIRCULAR RADIATION PATTERNS OF THE IDEAL ANTENNA MODEL AT POLAR ANGLE $\theta = 60^\circ$.

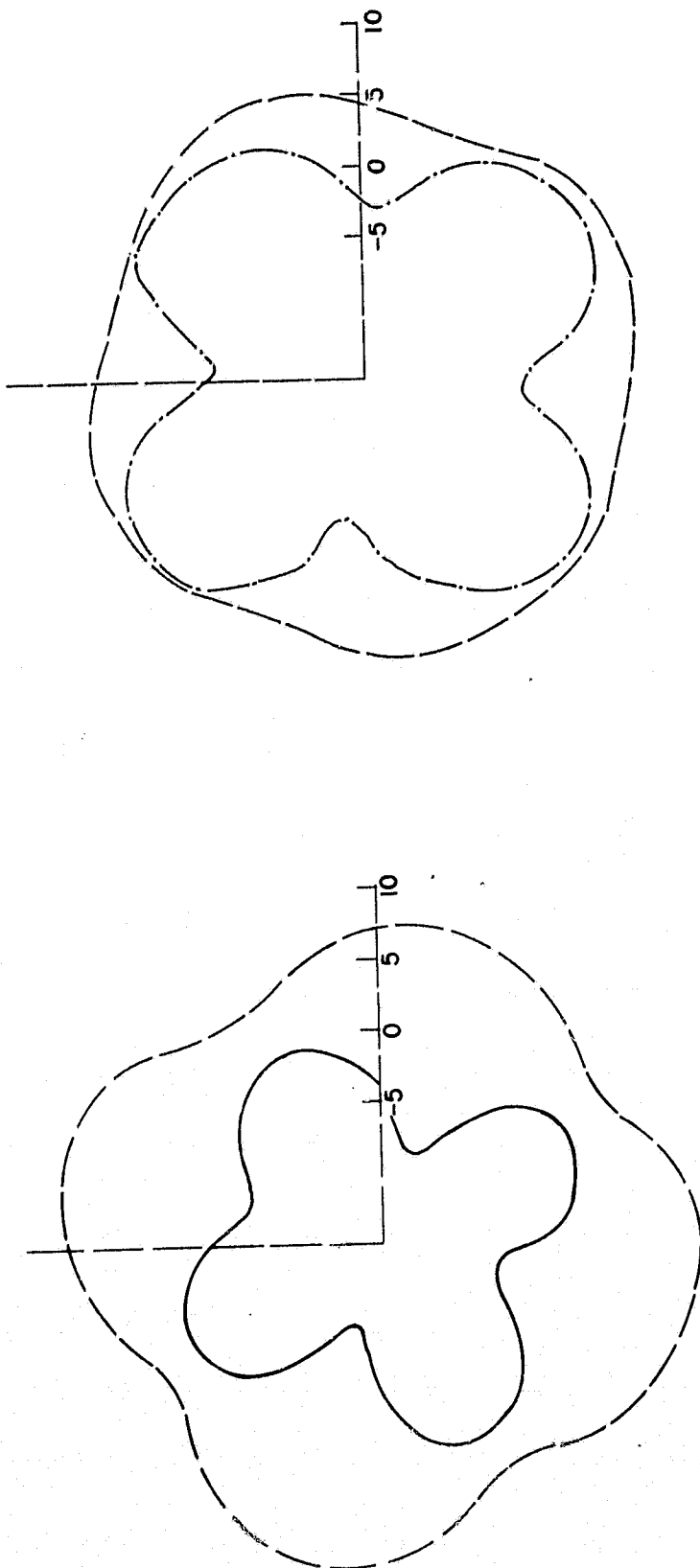


a. Linear



b. Circular

Fig. 12. SPACECRAFT LINEAR AND CIRCULAR RADIATION PATTERNS MEASURED BY GSFC AT POLAR ANGLE $\theta = 60^\circ$.



a. Linear

b. Circular

Fig. 13. SPACECRAFT LINEAR AND CIRCULAR RADIATION PATTERNS MEASURED BY GSFC IN THE EQUATORIAL PLANE $\theta = 90^\circ$.

which could be applied to the ideal model. The coefficients were chosen to make the average power radiated by the model equal to the average measured power over one spacecraft rotation. Averages were taken at $\theta = 60^\circ$, 75° , 90° , 105° , and 120° , which provided enough information to specify the five coefficients.

Because the distortions of the two linear polarizations were different, it was necessary to find two such scaling functions--one for E_θ and one for E_ϕ . The scaling functions found are given below and are plotted in Fig. 14.

$$f_\theta(\theta) = -19.47 \theta^4 + 140.28 \theta^3 - 366.27 \theta^2 + 407.05 \theta - 159.54 \quad (\text{A.20})$$

$$f_\phi(\theta) = 0.177 \theta^4 - 1.013 \theta^3 + 2.184 \theta^2 - 2.374 \theta + 2.040 \quad (\text{A.21})$$

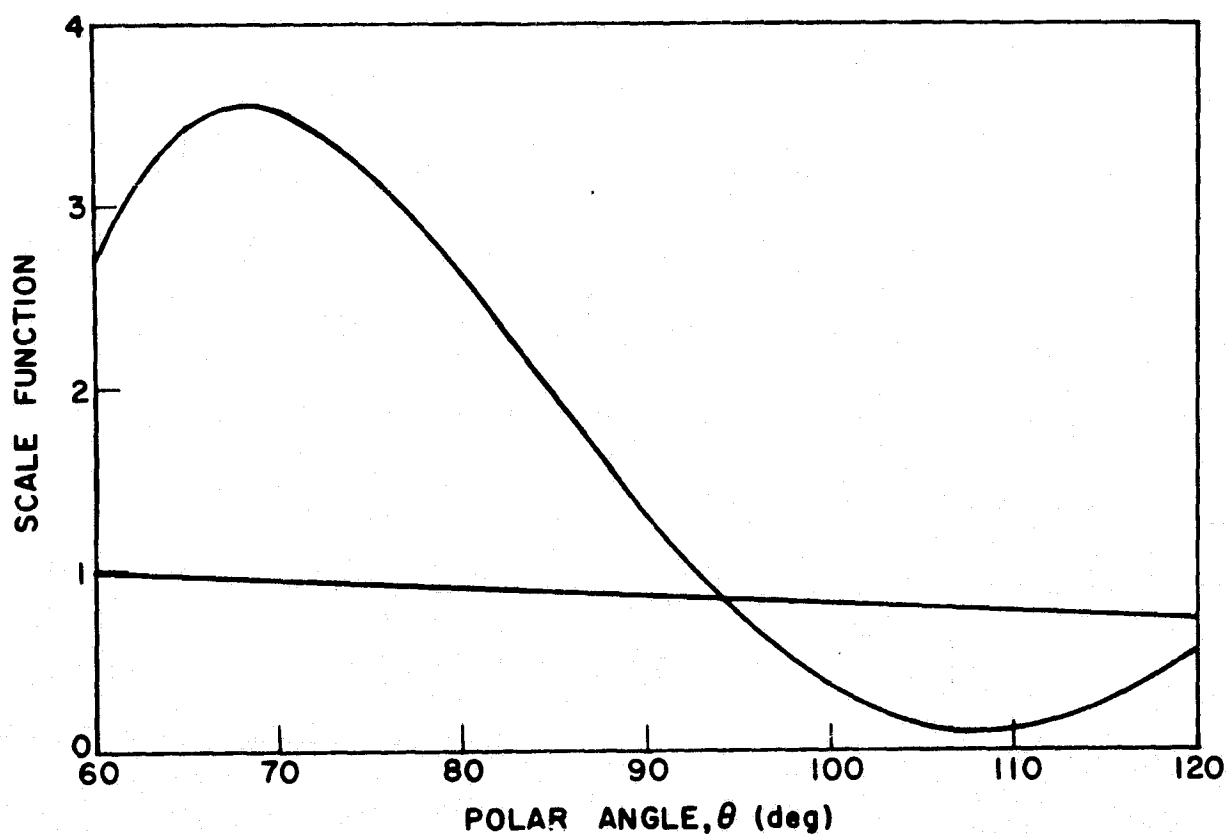


Fig. 14. SCALING FUNCTIONS USED TO COMPENSATE FOR DISTORTION BY SOLAR PANELS AND MAGNETOMETER BOOMS. Scaling accounted for polar but not rotational variations in the patterns. $f_\phi(\theta)$ is the nearly straight line.

The ideal model, scaled by the above functions, has been designated the " θ -scaled model." Linear radiation patterns are the same as those shown in Figs. 10 and 11 except for shrinkage or expansion due to the scaling.

Computation of the expected patterns for left and right circular polarizations from the θ -scaled model gave results which are shown in Figs. 15 and 16. Compared with the corresponding measured circular patterns these show agreement only if one rotates the model patterns with respect to the measured ones.

In general, the agreement between the computed and measured patterns for circular polarization was very poor. Since the model was believed to be correct, it was decided to check the measured patterns for internal consistency. This could be accomplished in a number of ways but the simplest appeared to be a point-by-point check of total power in the linear and circular patterns. Total power at any point should not depend on whether linear or circular antennas are used to measure it. In particular

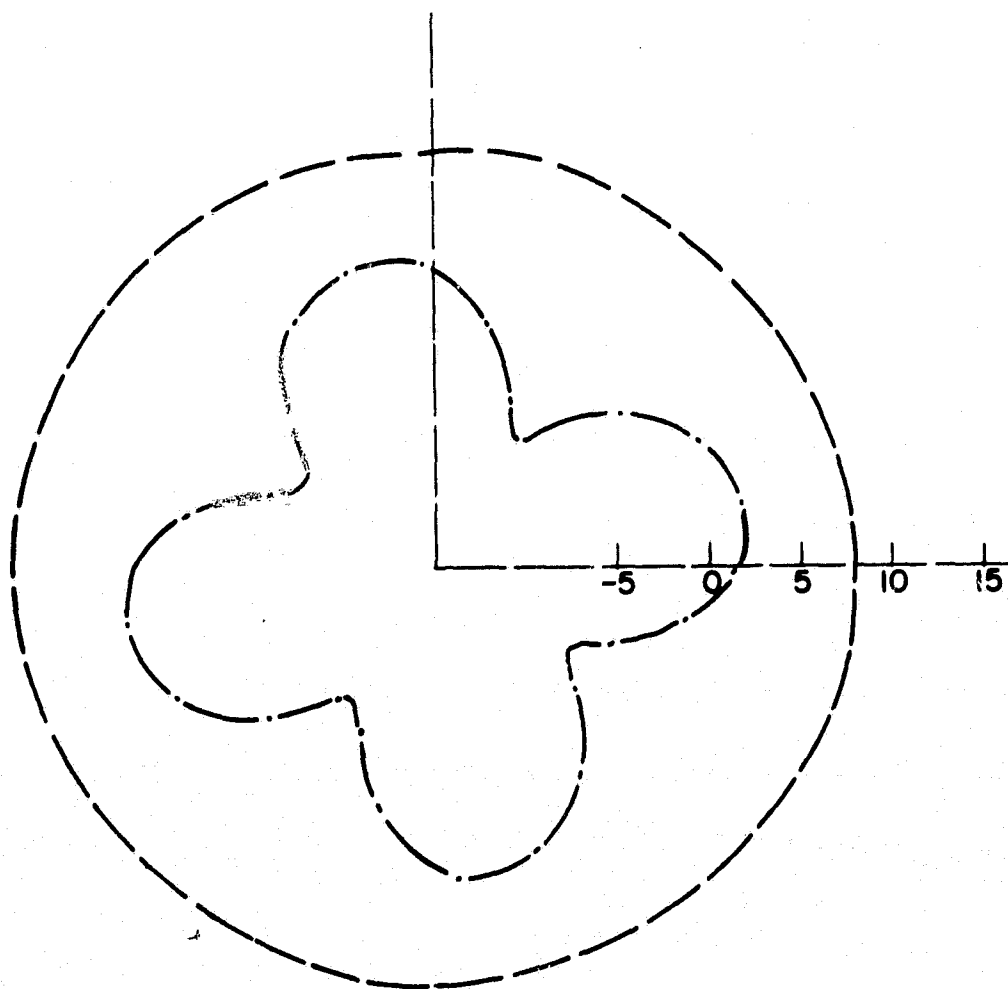


Fig. 15. CIRCULAR RADIATION PATTERN FROM THE θ -SCALED ANTENNA MODEL AT AN ANGLE OF $\theta = 60^\circ$.

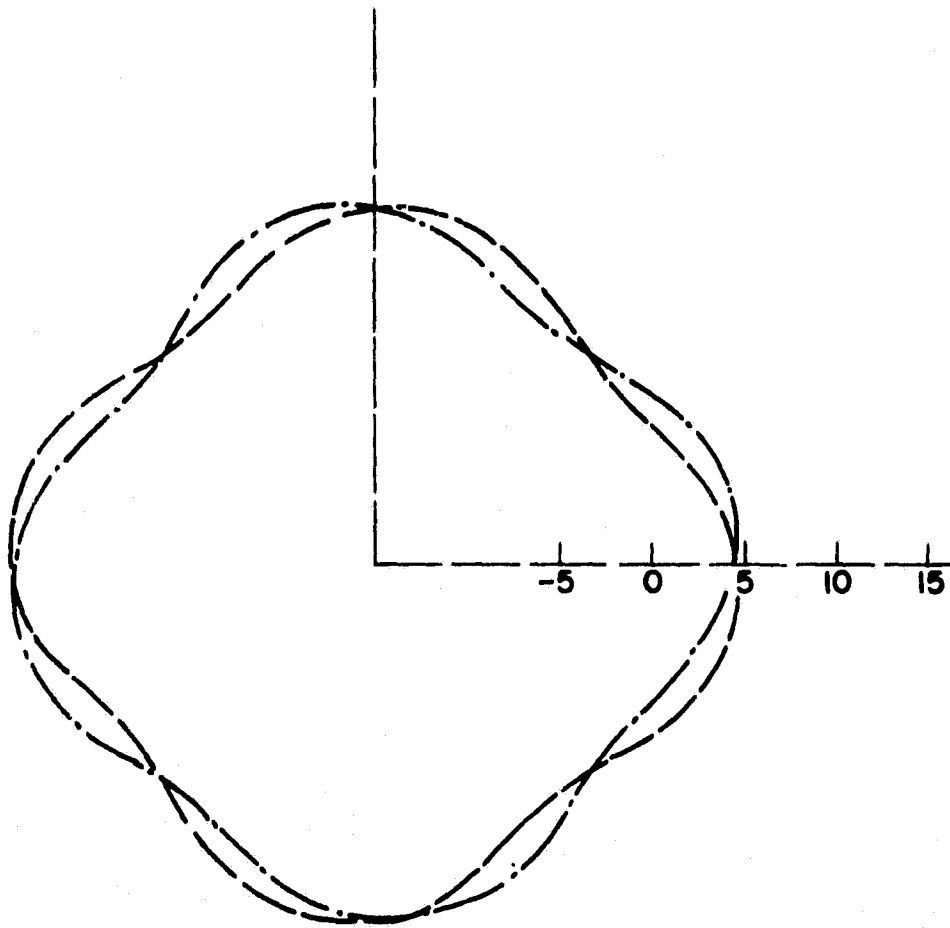


Fig. 16. CIRCULAR RADIATION PATTERN FROM THE θ -SCALED ANTENNA MODEL IN THE EQUATORIAL PLANE $\theta = 90^\circ$.

$$P_c(\theta, \phi) = P_L(\theta, \phi) \quad (\text{A.22})$$

where $P_c(\theta, \phi)$ is total circular power and $P_L(\theta, \phi)$ is total linear power measured at (θ, ϕ) . However, there was no reason to assume the gain of the circular antennas would be the same as the linear; allowing for this

$$\text{RAT}(\theta, \phi) = P_c(\theta, \phi) / P_L(\theta, \phi) \quad (\text{A.23})$$

should be constant--independent of (θ, ϕ) --over all space.

Using the values plotted on the GSFC linear and circular patterns, it was found that $\text{RAT}(\theta, \phi)$ was not constant (see Fig. 17); in fact, there was a 7 dB variation between high and low points. In addition,

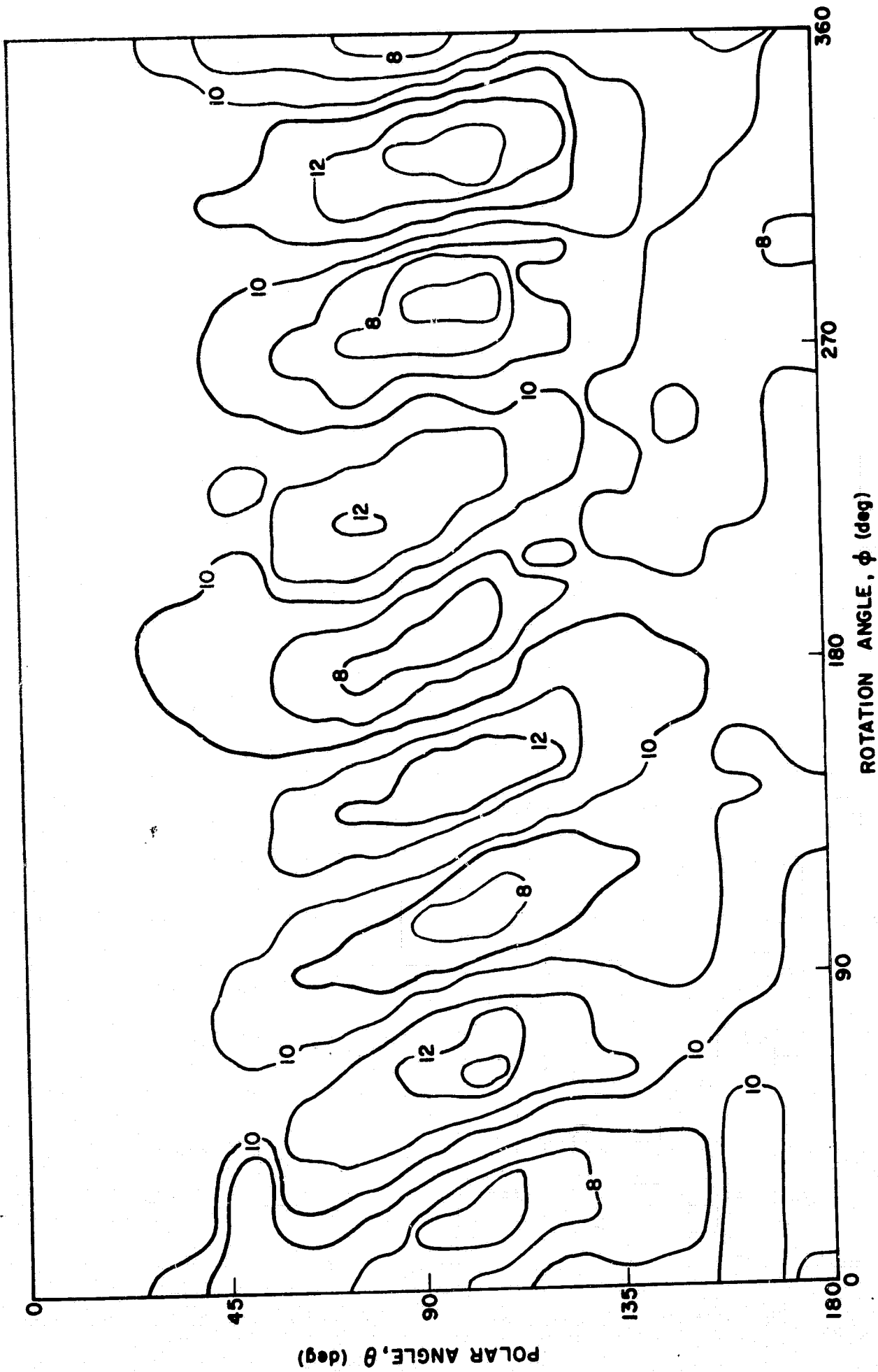


Fig. 17. RATIO OF MEASURED TOTAL CIRCULAR TO TOTAL LINEAR POWER TAKEN FROM THE GSFC-SUPPLIED PATTERNS AT ALL POLAR AND ROTATIONAL ANGLES. Contours are drawn on an arbitrary decibel scale in levels of 1 dB.

the variations appeared to be periodic, repeating every 90° . These fluctuations were most important in the belt from $\theta = 60^\circ$ to $\theta = 120^\circ$, the range over which almost all reflectivity measurements were made in this experiment.

Several possibilities for the discrepancy were considered, including coupling between orthogonal receiving systems, variations in gain, and mechanical errors in measurement resulting in an angular offset between the linear circular patterns. Consultation with GSFC brought assurance that the maximum error on any of the patterns was ± 1 dB--not enough to account for the variations. Since it was impossible to remeasure the spacecraft antenna pattern, this left a possible angular offset as the only other explanation suitable for testing.

A new function similar to $RAT(\theta, \phi)$ was generated:

$$RAT_{\phi_0} = \log_{10} \left[P_c(\theta, \phi - \phi_0) / P_L(\theta, \phi) \right] \quad (A.24)$$

That is, the circular patterns were offset by an amount ϕ_0 and the ratio of circular to linear power was again computed at each (θ, ϕ) point. Computation was performed for $0^\circ \leq \phi_0 \leq 360^\circ$ in 5° increments. Means and variances were obtained (see below) over all points (θ, ϕ) . It was found that an offset ϕ_0 between 45 and 50° provided the best fit in both standard and weighted cases (Fig. 18).

The mean and variance were computed from

$$\langle RAT_{\phi_0} \rangle = \sum_{\theta} \sum_{\phi} RAT_{\phi_0}(\theta, \phi) / N \quad (A.25)$$

$$\sigma^2 = \sum_{\theta} \sum_{\phi} \left[RAT_{\phi_0}(\theta, \phi) - \langle RAT_{\phi_0} \rangle \right]^2 / N \quad (A.26)$$

where N is the total number of (θ, ϕ) points considered

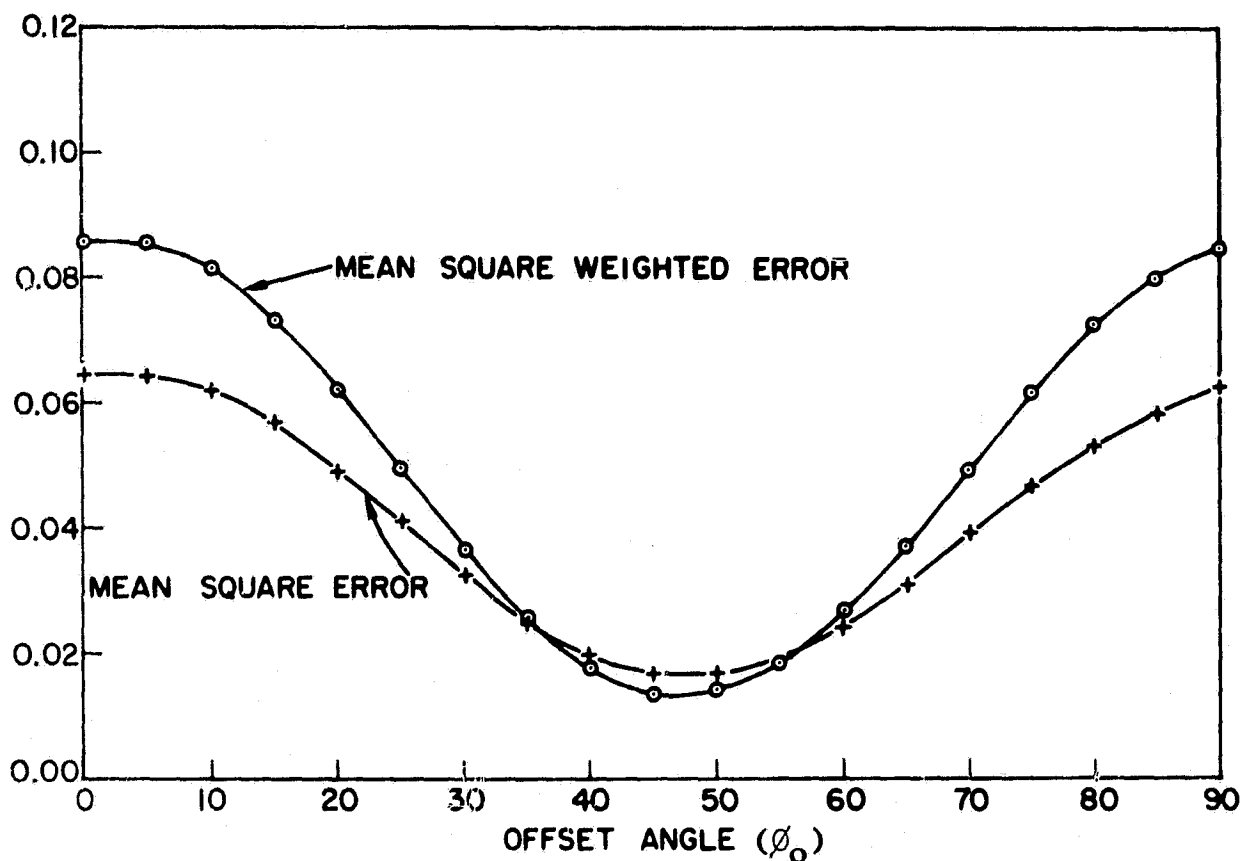


Fig. 18. VARIANCE PLOTTED AGAINST ANGLE AS THE CIRCULAR PATTERNS ARE ROTATED RELATIVE TO THE LINEAR PATTERNS.

$$N = \sum_{\theta} \sum_{\phi} 1 \quad (\text{A.27})$$

Since the (θ, ϕ) points become more dense near the poles of a spherical surface, the polar contribution will be disproportionately large with respect to the rest of the surface. To correct this, weighted averages and variances can be defined.

$$\langle \text{RAT}_{\phi_o, w} \rangle = \sum_{\theta} \sum_{\phi} \sin \theta \cdot \text{RAT}_{\phi_o}(\theta, \phi) / N_w \quad (\text{A.28})$$

$$\sigma_w^2 = \sum_{\theta} \sum_{\phi} \sin^2 \theta \left[\text{RAT}_{\phi_o}(\theta, \phi) - \langle \text{RAT}_{\phi_o, w} \rangle \right]^2 / N_w \quad (\text{A.29})$$

where N_w is the weighted number of points taken

$$N_w = \sum_{\theta} \sum_{\phi} \sin \theta \quad (\text{A.30})$$

A further possibility was that one set of patterns was upside down (flipped over) with respect to the other. To check this

$$\text{REV}_{\phi_0}(\theta, \phi) = P_c(\theta, -\phi - \phi_0) / P_L(\theta, \phi) \quad (\text{A.31})$$

was evaluated. An offset of 45° provided the best fit but the null was not nearly so deep as the one shown in Fig. 8. On this basis further work was restricted to simply finding one offset explanation.

At $\theta = 90^\circ$ the match between measured and model patterns was fairly convincing; however, at other polar angles it appeared less satisfactory. If the circular patterns had been offset by different amounts at different θ the matches might have been better. Under these conditions the 45° offset would have merely represented an average.

To test this progressive offset hypothesis

$$P_c(\theta, \phi - \phi_0) / P_L(\theta, \phi)$$

was calculated at each θ and the best offset was found. Figure 19 shows the results along with an indication of the sharpness of the fit.

The progressive offset correction is presently accepted as the means to produce the best matching between measured and model patterns. It appears that a linear slippage of either the antenna or the recording instrument occurred during measurement of the circular antenna patterns. If a rate of 7.5° of rotational slippage for each 15° polar increment is assumed, the shape of the ideal model curves matches the shape of the measured curves fairly closely.

With the offset problem resolved interest could return to modeling the antenna. Whereas the θ -scaled model adjusted amplitudes only as a

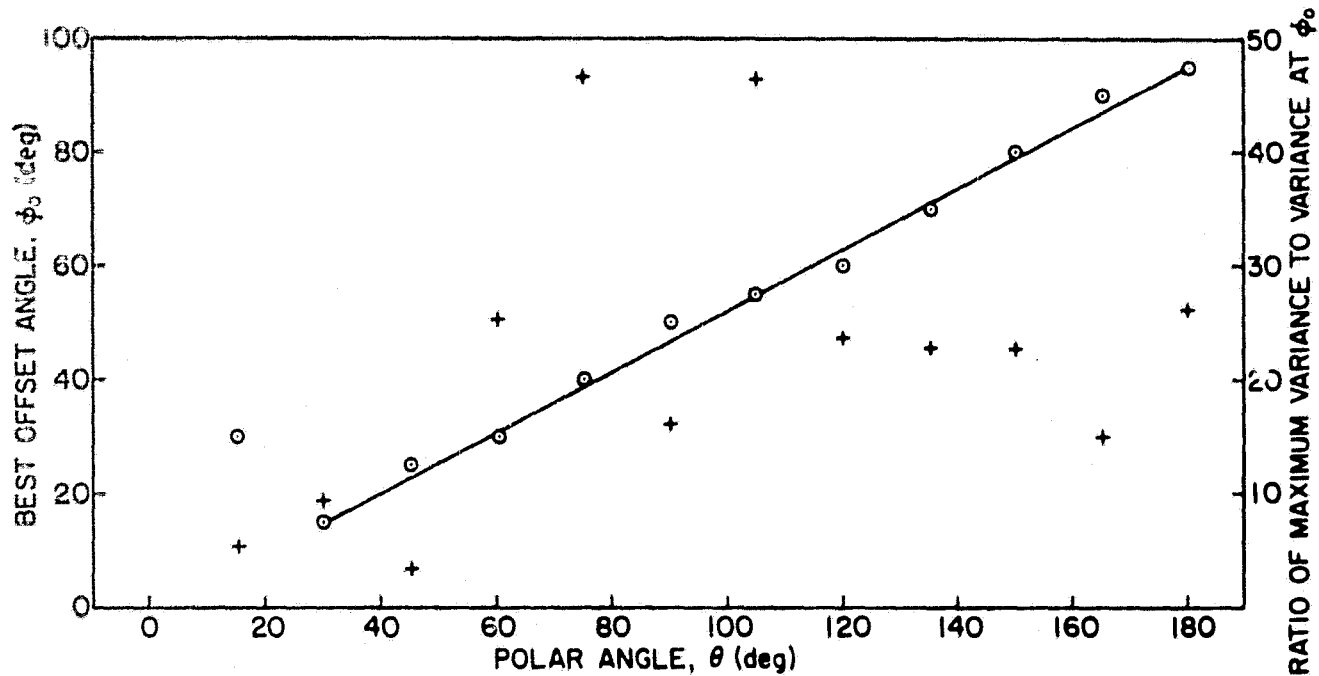


Fig. 19. BEST OFFSET ANGLE AS A FUNCTION OF θ . Circles indicate best angular fit and crosses are the ratio of the maximum to minimum variances. High ratios correlate with good fits at the indicated angle; low ratios mean that the exact rotation is not critical. A straight line has been drawn through the offsets for $30^\circ \leq \theta \leq 180^\circ$.

function of θ it was now felt desirable to consider rotational variations. Two arrays of 864 elements were formed giving the ratio of measured field to ideal model field in 15° increments of polar angle and 5° increments of rotation. One array was used for the θ -component of the field and the other for the ϕ -component. Computation of the circular fields for this "array-scaled model" gave patterns as shown in Figs. 20 and 21. A subjective fit of these patterns to those shown in Figs. 12 and 13 shows good agreement, provided the proper offset is introduced. The array-scaled model is now accepted as being equivalent to the Explorer 35 antenna, insofar as the radiation patterns are concerned.

3. Choice of Coordinate Frame, Poincaré Parameters

Having synthesized the spacecraft radiation, it now becomes necessary to consider how the field interacts with the surface. Because of

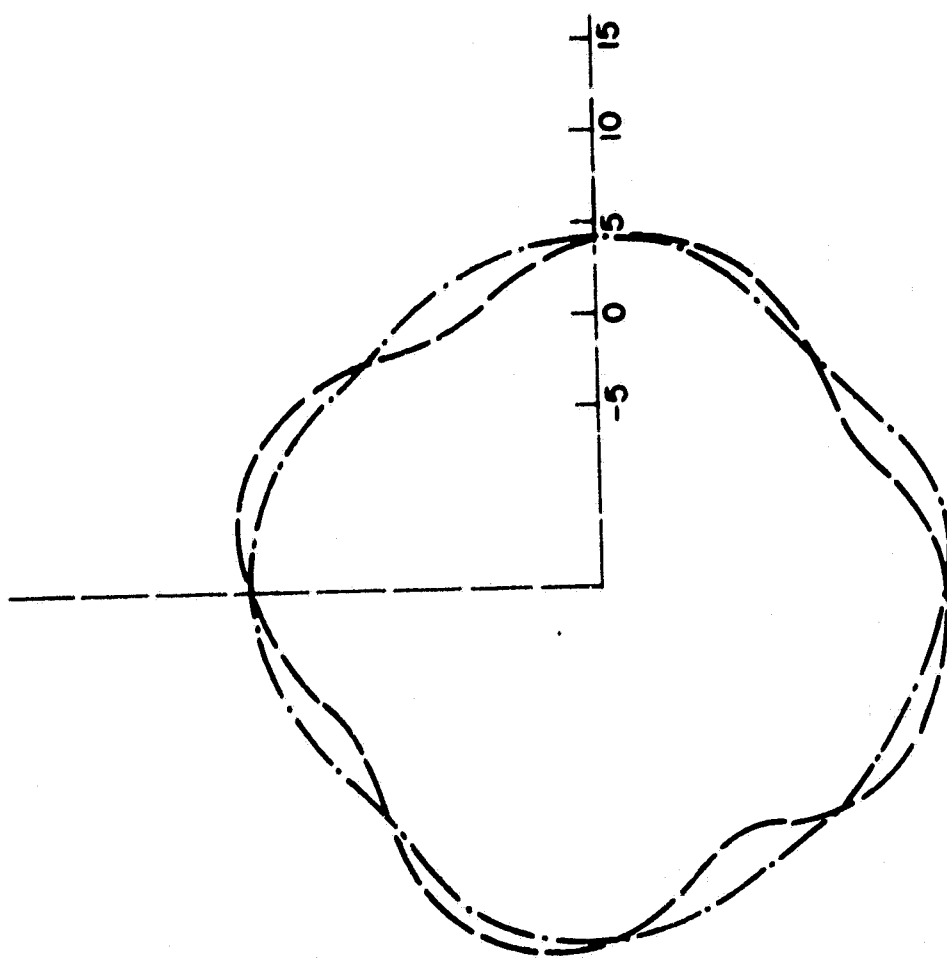


Fig. 21. CIRCULAR RADIATION PATTERN CALCULATED FOR THE ARRAY-SCALED MODEL IN THE EQUATORIAL PLANE $\theta = 90^\circ$.

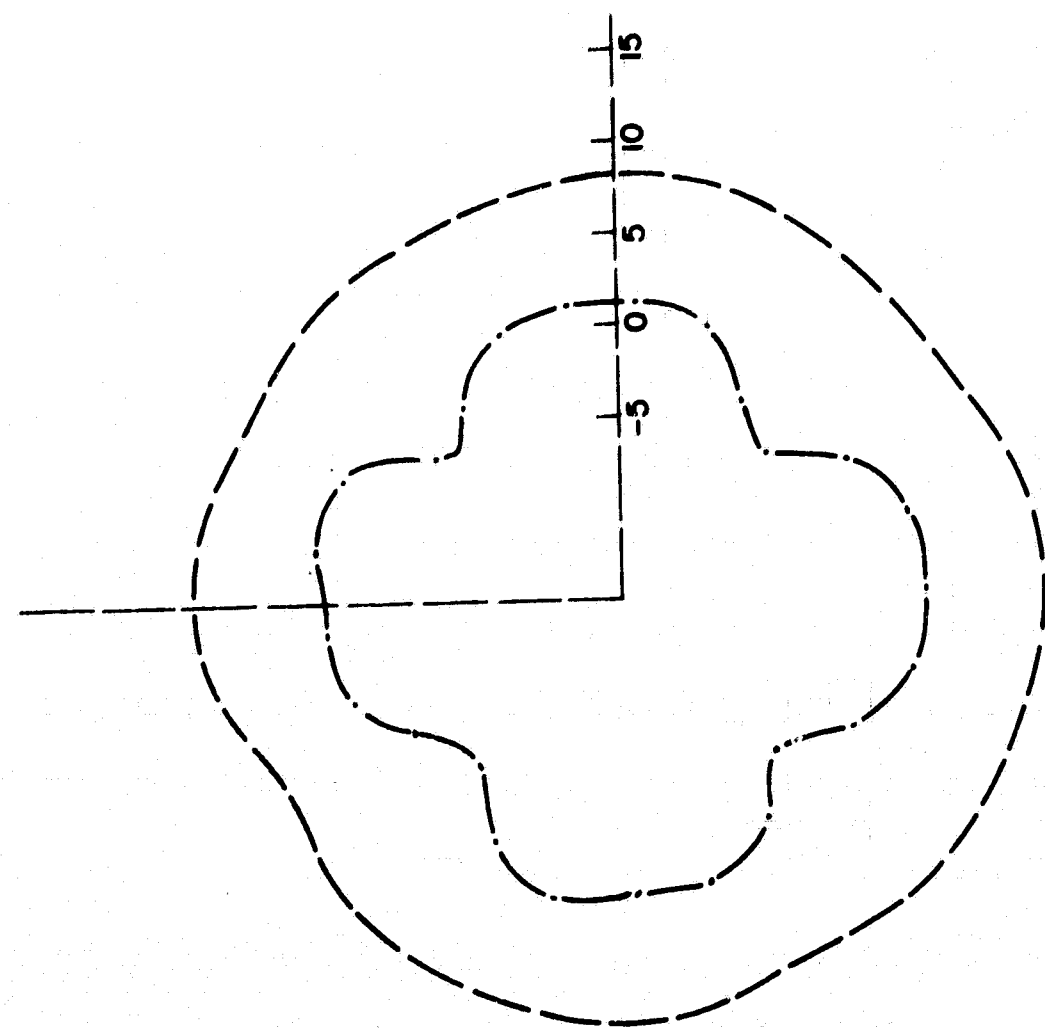


Fig. 20. CIRCULAR RADIATION PATTERN CALCULATED FOR THE ARRAY-SCALED MODEL AT $\theta = 60^\circ$.

the different coordinate systems associated with the spacecraft, the lunar surface, and the receiving set-up, Poincaré parameters are a convenient way to describe the incident and reflected waves. Poincaré parameters allow relatively easy conversion from one coordinate system to another even when the geometry is time-varying. A brief discussion of the method used to obtain the Poincaré parameters follows.

The system of coordinates is defined as shown in Fig. 22. \bar{k} is the wave vector and points in the direction of propagation. Right rotational polarization is defined such that, in a fixed plane, $\bar{E}(t)$ rotates clockwise when looking in the direction of \bar{k} . Figure 22 shows some of the variables to be used.

M = length of the semi-major axis of the polarization ellipse

N = length of the semi-minor axis

\bar{E}_m = vector of the maximum \bar{E} ($M = |\bar{E}_m|$)

γ_0 = angle between \bar{E}_m and \bar{a}_θ

\bar{a}_θ , \bar{a}_ϕ , and \bar{k} define an orthogonal right-hand coordinate system.

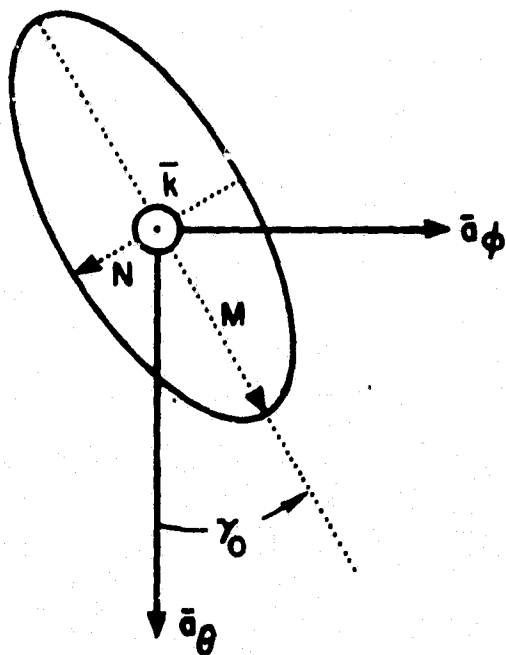


Fig. 22. THE POLARIZATION ELLIPSE SHOWING QUANTITIES OF INTEREST. $\bar{a}_\theta \times \bar{a}_\phi = \bar{k}$ is the direction of propagation.

If one considers the E-field to be made up of θ - and ϕ -components with real and imaginary parts, these components may be expressed as

$$E_{\theta} = A + jB \quad (\text{A.32})$$

$$E_{\phi} = C + jD \quad (\text{A.33})$$

Phasor notation is often more convenient so the above may be given alternatively by

$$E_{\theta} = (A^2 + B^2)^{1/2} e^{j\alpha} \quad \alpha = \arctan (B/A) \quad -\pi \leq \alpha \leq \pi \quad (\text{A.34})$$

$$E_{\phi} = (C^2 + D^2)^{1/2} e^{j\beta} \quad \beta = \arctan (D/C) \quad -\pi \leq \beta \leq \pi \quad (\text{A.35})$$

Absolute phase is not of any importance so a relative phase difference between the θ - and ϕ -components may be used

$$\delta = \beta - \alpha \quad -\pi \leq \delta \leq \pi \quad (\text{A.36})$$

where

$$E_{\theta} = (A^2 + B^2)^{1/2} \quad (\text{A.37})$$

$$E_{\phi} = (C^2 + D^2)^{1/2} e^{j\delta} \quad (\text{A.38})$$

It is possible to decompose any linear vector into two oppositely rotating circular vectors of equal amplitude. Using the superscripts R and L to designate right and left circular, one obtains

$$E_{\theta}^R = \frac{1}{2} (A^2 + B^2)^{1/2} \quad (\text{A.39})$$

$$E_{\theta}^L = \frac{1}{2} (A^2 + B^2)^{1/2} \quad (\text{A.40})$$

$$E_{\phi}^R = \frac{1}{2} (C^2 + D^2)^{1/2} e^{j\delta} \quad (\text{A.41})$$

$$E_{\phi}^L = \frac{1}{2} (C^2 + D^2)^{1/2} e^{j\delta} \quad (\text{A.42})$$

Addition of contributions of similar senses gives the total right and left circular vectors (positive δ means the ϕ contribution leads the θ contribution in time). This is shown in Figs. 23 and 24.

$$\bar{E}^R = \frac{1}{2} (A^2 + B^2)^{1/2} \bar{a}_{\theta} - \frac{1}{2} (C^2 + D^2)^{1/2} (\sin \delta) \bar{a}_{\theta} + \frac{1}{2} (C^2 + D^2)^{1/2} (\cos \delta) \bar{a}_{\phi} \quad (\text{A.43})$$

$$\bar{E}^L = \frac{1}{2} (A^2 + B^2)^{1/2} \bar{a}_{\theta} + \frac{1}{2} (C^2 + D^2)^{1/2} (\sin \delta) \bar{a}_{\theta} + \frac{1}{2} (C^2 + D^2)^{1/2} (\cos \delta) \bar{a}_{\phi} \quad (\text{A.44})$$

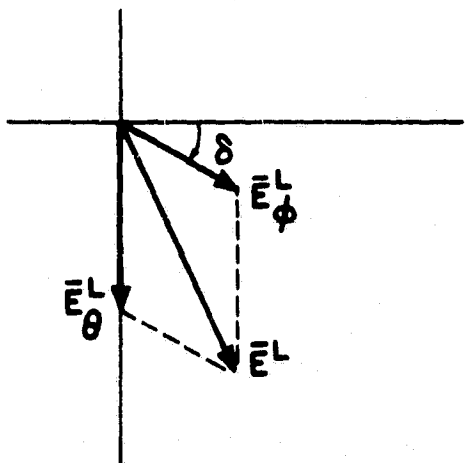


Fig. 23. θ AND ϕ CONTRIBUTIONS ADD TO GIVE A TOTAL LEFT CIRCULAR VECTOR.

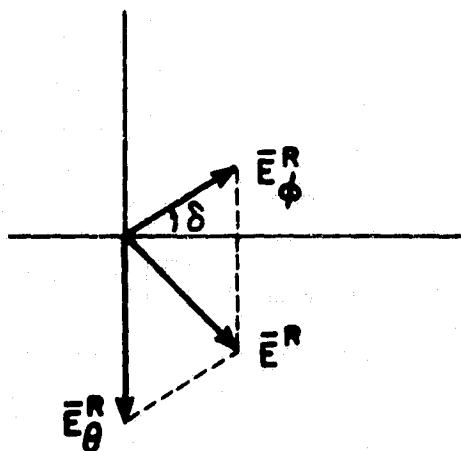


Fig. 24. θ AND ϕ CONTRIBUTIONS ADD TO GIVE A TOTAL RIGHT CIRCULAR VECTOR.

The maximum E-field, \bar{E}_m , will occur when \bar{E}^R and \bar{E}^L coincide; minimum E-field occurs when they oppose each other. Thus

$$M = |\bar{E}^L| + |\bar{E}^R| \quad (\text{A.45})$$

$$N = |\bar{E}^L| - |\bar{E}^R| \quad (\text{A.46})$$

Given A, B, C, and D, it is possible to evaluate the first Poincaré parameter, χ_0 , from its definition

$$\tan \chi_0 \triangleq \frac{N}{M} \quad (\text{A.47})$$

A second parameter is γ_0 , the angle between \bar{E}_m and \bar{a}_θ . Since \bar{E}^R and \bar{E}^L rotate at the same angular rate (albeit with different magnitudes and directions), γ_0 equals half the angle between \bar{E}^R and \bar{E}^L added to the angle \bar{E}^R makes with \bar{a}_θ (see Fig. 25). That is

$$\gamma_0 = \arccos \frac{\bar{a}_\theta \cdot \bar{E}^R}{|\bar{E}^R|} + \frac{1}{2} \arccos \frac{\bar{E}^R \cdot \bar{E}^L}{|\bar{E}^R| |\bar{E}^L|} \quad 0 \leq \gamma_0 \leq \pi \quad (\text{A.48})$$

The third parameter is simply a measure of intensity. It is defined as

$$S_0 = |\bar{E}_\theta|^2 + |\bar{E}_\phi|^2 = A^2 + B^2 + C^2 + D^2 \quad (\text{A.49})$$

The field of the model antenna is specified by the quantities A, B, C, and D so it is possible to determine the Poincaré parameters of the incident wave on the surface.

The scattering surface will in general be tilted at some arbitrary angle with respect to the incoming wave vector. To understand scattering by the surface one must convert incident and reflected Poincaré parameters to values relative to the surface. S , γ , and χ will be used to designate Poincaré parameters of the incident wave at the surface.

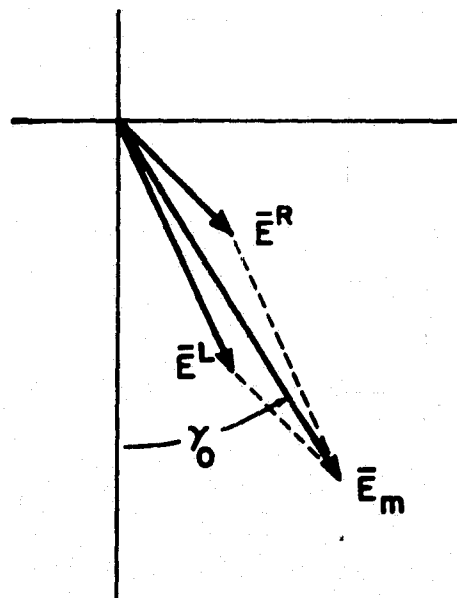


Fig. 25. \bar{E}^L AND \bar{E}^R COINCIDE AT γ_0 TO PRODUCE THE MAXIMUM ELECTRIC VECTOR \bar{E}_m .

S will depend on the distance between the spacecraft and the scattering point, or

$$S = S_0/r^2 \quad (\text{A.50})$$

The sense of rotation and the lengths of the semimajor and semiminor axes of the polarization ellipse will not change so long as the medium does not become overly pathological, and

$$\chi = \chi_0 \quad (\text{A.51})$$

The angle the semimajor axis makes with \bar{a}_θ will not change, but to discuss scattering at the surface one must know the angle between the semimajor axis and some reference on the surface (we chose the horizon). Hence

$$\gamma = \gamma_g + \gamma_0 \quad (\text{A.52})$$

where γ_g is the geometrical correction between \bar{a}_θ and the horizon. The following definitions will be used.

\bar{a}_θ = unit vector in the θ direction with respect to the spacecraft

\bar{S} = spin vector of the spacecraft

\bar{D} = vector from the spacecraft to the scattering point

\bar{B} = vector from the Moon's center to the scattering point

$\bar{n} = \bar{B}/|\bar{B}|$ = unit normal to the mean surface at the scattering point

\bar{P} = vector from the Moon's center to the spacecraft.

By definition $\bar{a}_\theta \cdot (\bar{D} \times \bar{a}_\theta) = 0$. From this and the fact that \bar{a}_θ is in a plane perpendicular to $\bar{D} \times \bar{S}$, it is possible to define \bar{a}_θ in terms of \bar{D} and \bar{S} .

$$\bar{a}_\theta = \bar{D} \times (\bar{D} \times \bar{S}) / |\bar{D} \times (\bar{D} \times \bar{S})| \quad (\text{A.53})$$

The vector $\bar{B} \times \bar{D}$ is parallel to the horizon (since it is perpendicular to \bar{B}) and in the plane of the polarization ellipse (since it is perpendicular to \bar{D}). The corresponding unit vector may be defined as

$$\bar{h} = \bar{B} \times \bar{D} / |\bar{B} \times \bar{D}| \quad (\text{A.54})$$

The angle ψ can be defined (see Figs. 26 and 27) as

$$\psi = \arccos \left\{ \frac{\bar{S} \times \bar{D}}{|\bar{S} \times \bar{D}|} \cdot \frac{\bar{B} \times \bar{D}}{|\bar{B} \times \bar{D}|} \right\} \quad -\pi \leq \psi \leq \pi \quad (\text{A.55})$$

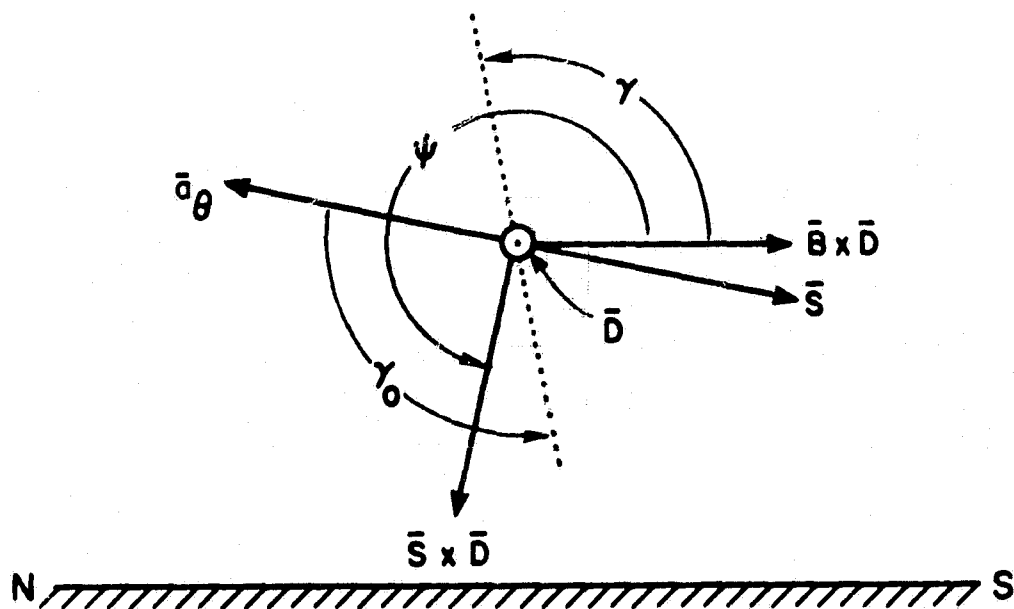


Fig. 26. FROM THE LUNAR EQUATOR EXPLORER 35 APPEARS TO RISE IN THE EAST WITH SPIN VECTOR \bar{S} POINTED GENERALLY SOUTH. \bar{D} is assumed perpendicular to \bar{S} for this simplified equatorial view.

Then the angle between \bar{a}_θ and \bar{h} is $\psi - \pi/2$. The principle value of γ_0 is between 0 and 180°, so is always positive. If γ is defined to be the angle between the semimajor axis of the ellipse and the local horizon, then

$$\gamma = \psi + \gamma_0 - 90^\circ \quad (\text{A.56})$$

Figure 26 is an example showing Explorer 35 just above the eastern lunar horizon. Here $\gamma_0 \approx 110^\circ$ and $\psi \approx -100^\circ$. This means $\gamma \approx -100^\circ + 110^\circ - 90^\circ = -80^\circ$ or, converting to principal values, $\gamma \approx 100^\circ$. Figure 27 shows the spacecraft over the western horizon. Assuming $\gamma \approx 110^\circ$ again and noting $\psi \approx 80^\circ$ now, one finds $\gamma \approx 80^\circ + 110^\circ - 90^\circ \approx 100^\circ$, as before.

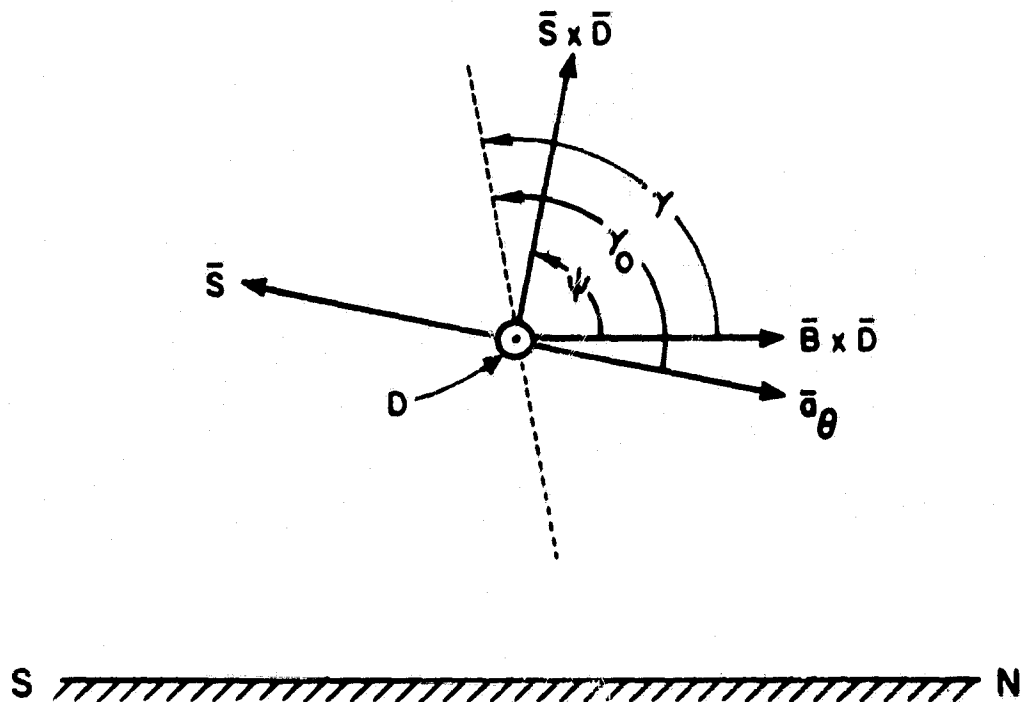


Fig. 27. THE SPACECRAFT APPEARS TO SET IN THE WEST WITH THE SPIN VECTOR STILL POINTING SOUTH. This figure and Fig. 26 show that both γ and γ_0 are constant as the spacecraft passes overhead so long as the spin axis remains perpendicular to the line of sight.

4. Spacecraft Rotation, Averages of Fields and Poincaré Parameters

Explorer 35 rotates about its spin axis approximately once every two seconds resulting in a noticeable low-frequency fade on the received signal. In processing, data is Fourier transformed at a rate proportional to the sampling frequency [see Tyler, 1969] where the smallest time increment encountered corresponds to about 150° of spacecraft rotation. In general, some 60 to 120 sec of data is averaged, so the signal

observed is an average over many spacecraft rotations. Future work, however, may involve study of data over the minimum time increment. Concern over the 150° average vs a 360° average and uncertainty regarding the relationship between average Poincaré parameters and average fields prompted the next phase of work, a brief recount of which follows.

The Poincaré parameters S_0 and χ_0 , which depend only on the magnitude of the field components, can be obtained directly from the measured antenna patterns. On the other hand, γ_0 is phase dependent so one must revert to the antenna model.

S_0 is a measure of radiated power and is simply proportional to the sum of the powers in two orthogonal components

$$S_0 \sim |\bar{E}_\theta|^2 + |\bar{E}_\phi|^2 = P_\theta + P_\phi \quad (\text{A.57})$$

Figure 28 is a plot of S_0 vs rotation angle for both the ideal and array-scaled models in the equatorial ($\theta = 90^\circ$) plane of the spacecraft. By definition S_0 for the measured pattern is the same as for the array-scaled model.

The definition of χ was given in Eq. (A.47). For patterns given in decibels this translates directly to

$$\tan \chi = - \frac{1 - 10^{(\text{LHCDB}-\text{RHCDB})/20}}{1 + 10^{(\text{LHCDB}-\text{RHCDB})/20}} \quad (\text{A.58})$$

where LHCDB and RHCDB are the measured circular powers in decibels.

χ can also be computed directly from the fields and this has been done for both the ideal and array-scaled models. Figures 29 and 30 show χ plotted against RHCDB-LHCDB at four important polar angles. Results are very close to what would be obtained from Eq. (A.58).

Plotted against the angle of rotation, ϕ , χ shows an approximately sinusoidal variation with a period of 90°. In the equatorial plane (Fig. 31) the average field is linear while at $\theta = 75^\circ$ the field can be decomposed into two components--80 percent of the average field is linear and the rest is left circular.

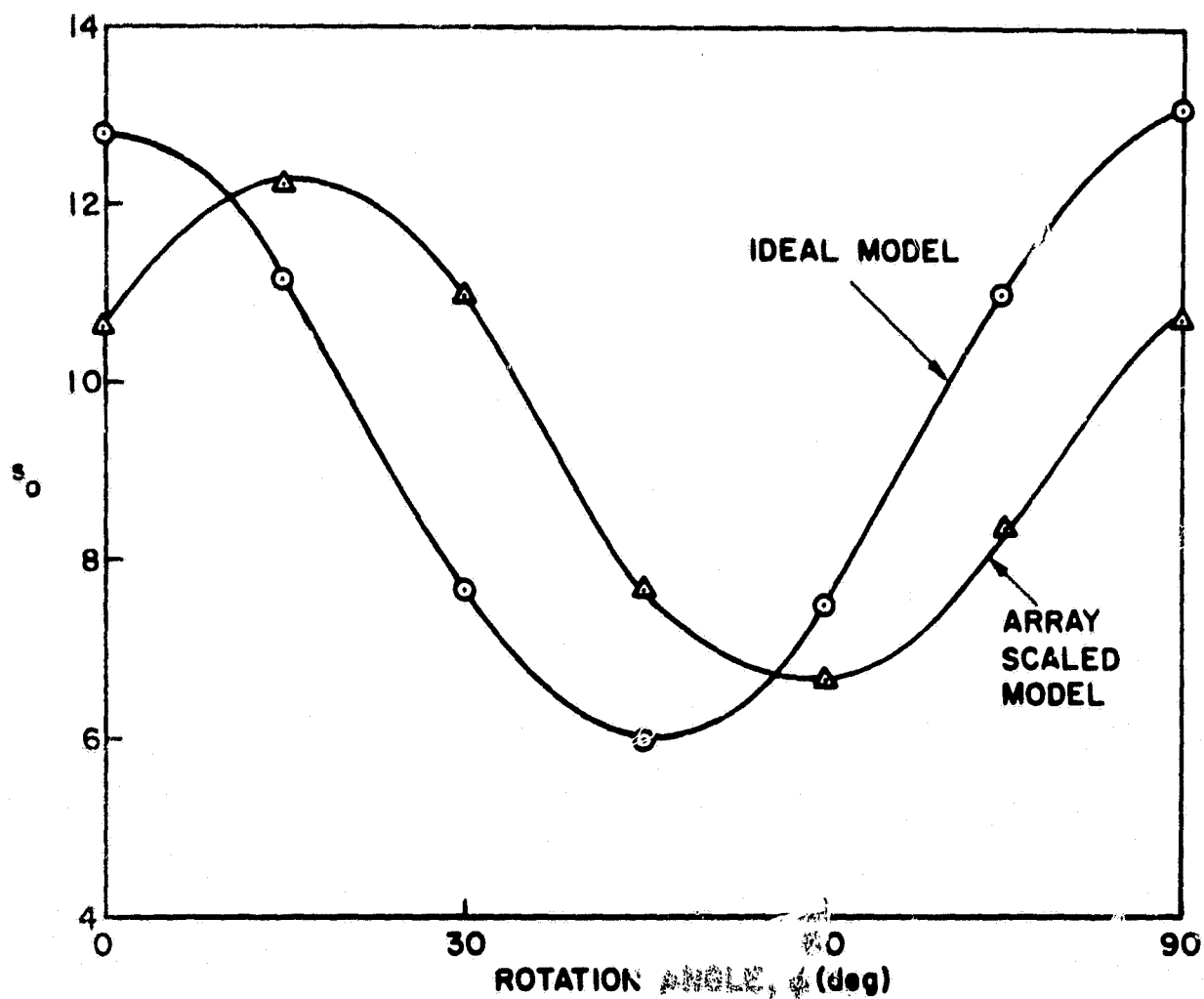
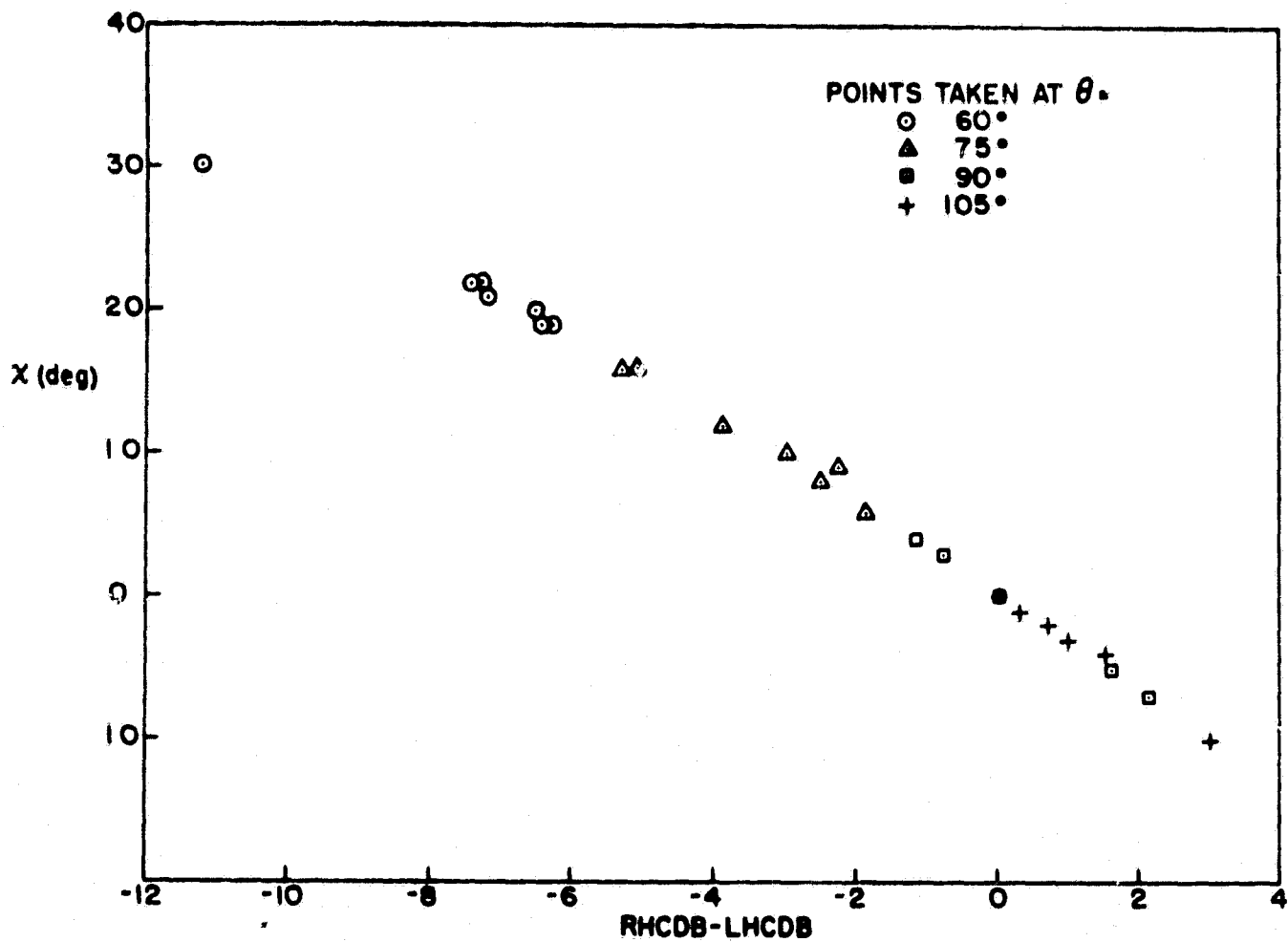


Fig. 28. POINCARÉ POWER PARAMETER S_0 PLOTTED AGAINST ROTATION ANGLE FOR BOTH THE IDEAL AND ARRAY-SCALED MODELS.

As before, the Poincaré parameter γ_0 is the most difficult to handle. This quantity gives the orientation of the polarization ellipse relative to the \bar{a}_θ direction in the spacecraft frame of reference. If γ_0 remains stable over a rotation of the spacecraft, the polarization ellipse of the incident wave on the surface remains fixed and the reflected wave will be readily determined.

An empirical plot of γ_0 points vs PHDB-THDB, the difference between the E_ϕ and E_θ powers measured in decibels, made for the array-scaled model is shown in Fig. 32. Points were plotted for a number of different polar angles. Although most points fall on what appears to be a broad arc, this result is misleading--there is a considerable scatter of points at all azimuths, so that γ_0 actually traces out a rather



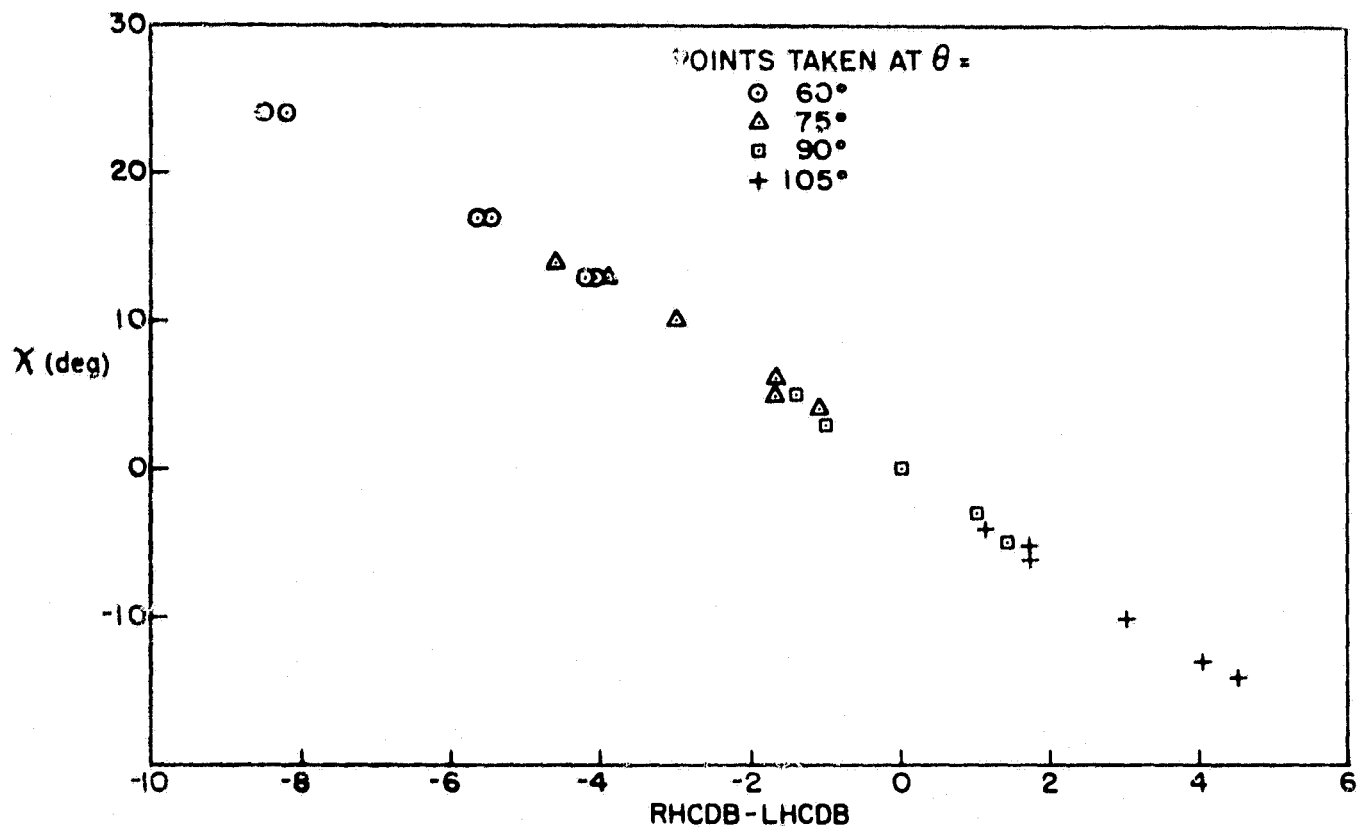


Fig. 30. χ VS RIGHT MINUS LEFT CIRCULAR POWERS IN DECIBELS FOR THE ARRAY-SCALED MODEL.

azimuthal angle in Fig. 35; it is clear that over the range of particular interest in this experiment ($60^\circ \leq \theta \leq 120^\circ$) there is little difference between averaging the fields and averaging the parameters.

The final problem to be considered was the effect of averaging over 150° of rotation rather than 360° . Figures 36, 37, and 38 show averages of S_o , γ_o , and χ_o over 360° with error bars indicating the maximum divergences encountered when averaging over the smaller range. The 150° intervals were chosen such that the average was over $\phi_o \leq \phi < \phi_o + 150^\circ$ where $\phi_o = 0^\circ, 15^\circ, 30^\circ, \dots, 360^\circ$. As can be seen, within the range of interest, the deviations resulting from only a partial average appear to be negligible.

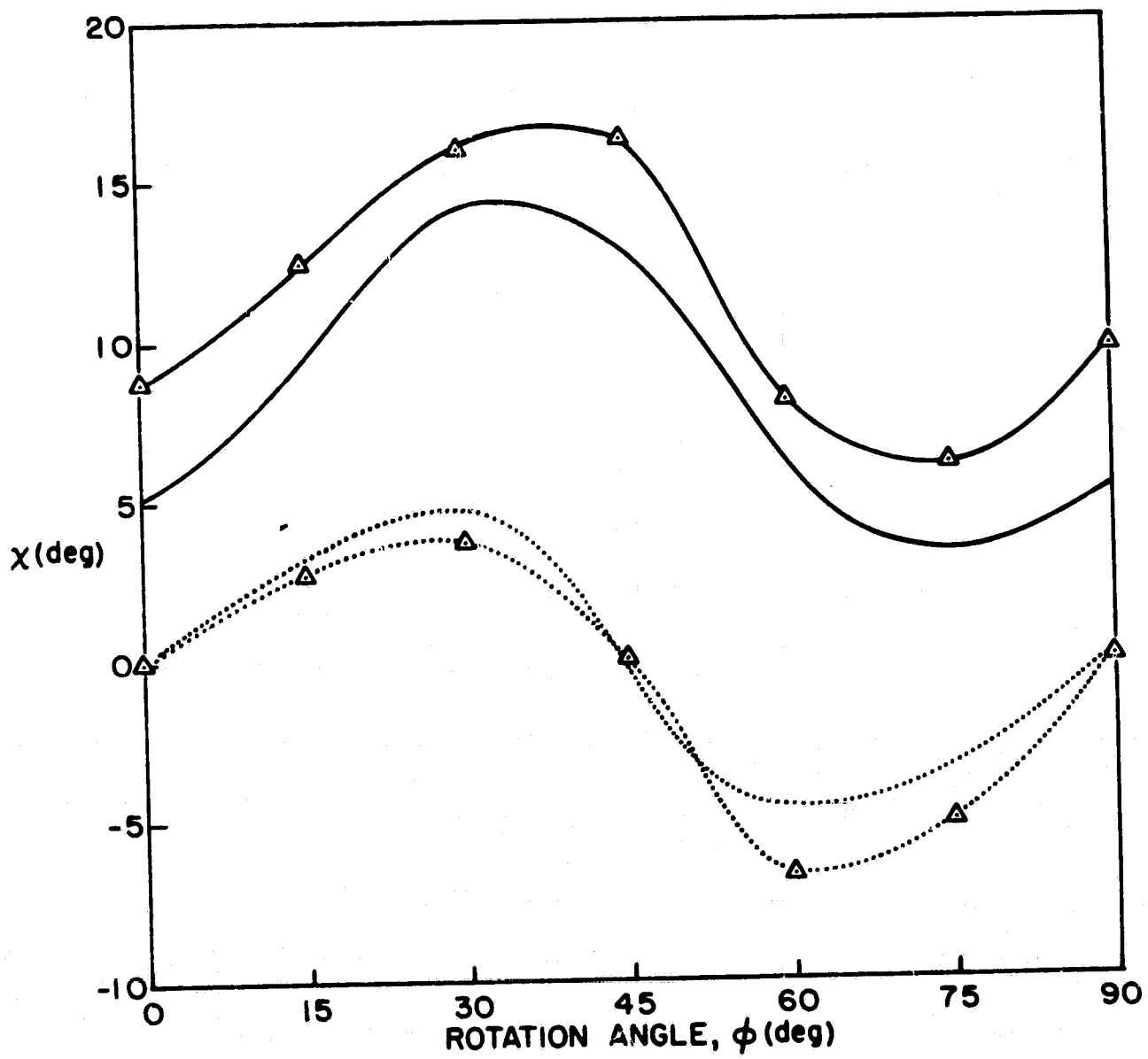


Fig. 31. VARIATIONS IN χ FOR THE IDEAL AND ARRAY-SCALED MODELS OVER 90° OF SPACECRAFT ROTATION. Solid lines are for $\theta = 60^\circ$; dotted lines for $\theta = 90^\circ$. Triangles indicate the array-scaled model.

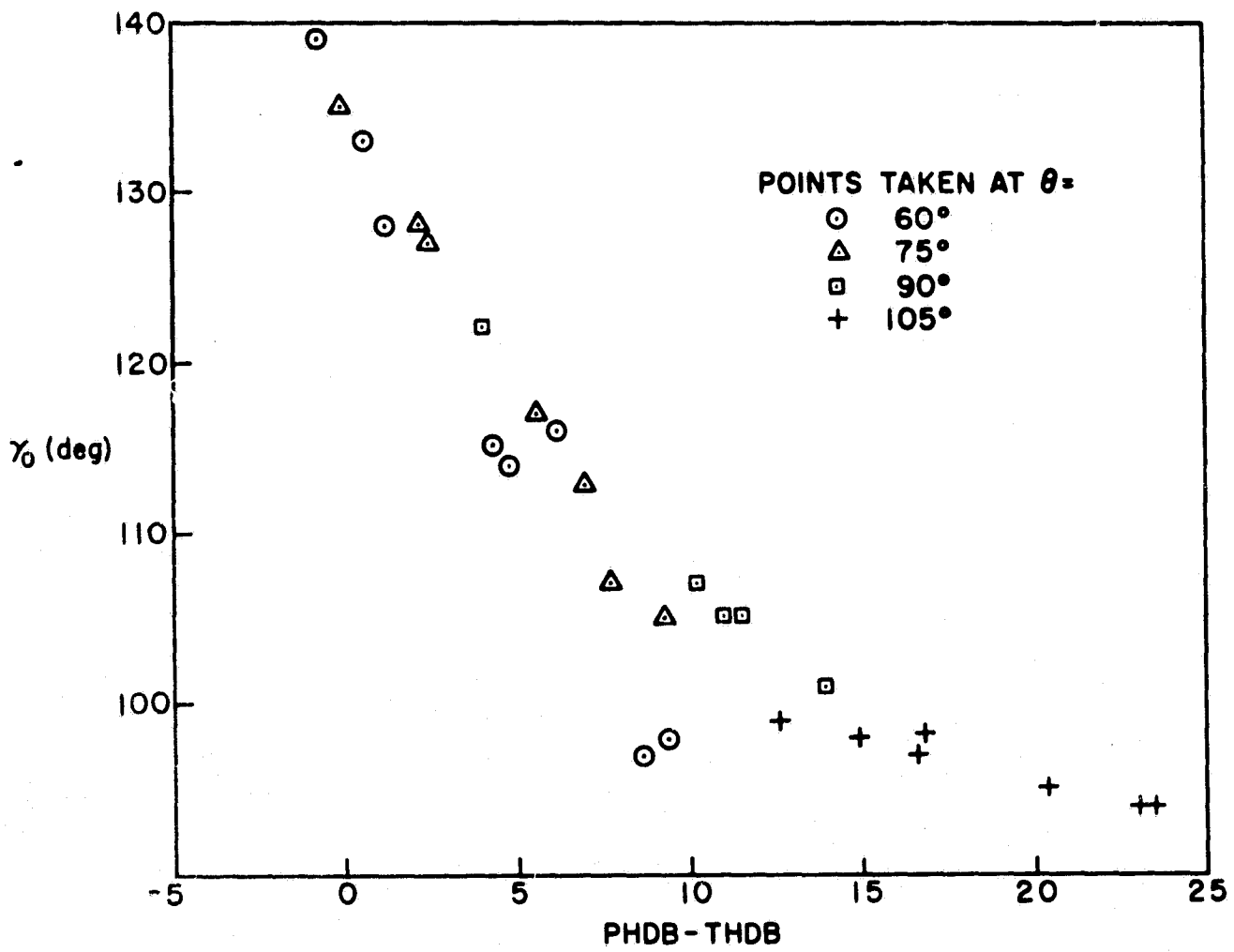


Fig. 32. γ_0 VS ϕ MINUS θ LINEAR POWERS IN DECIBELS FOR THE ARRAY-SCALED MODEL.

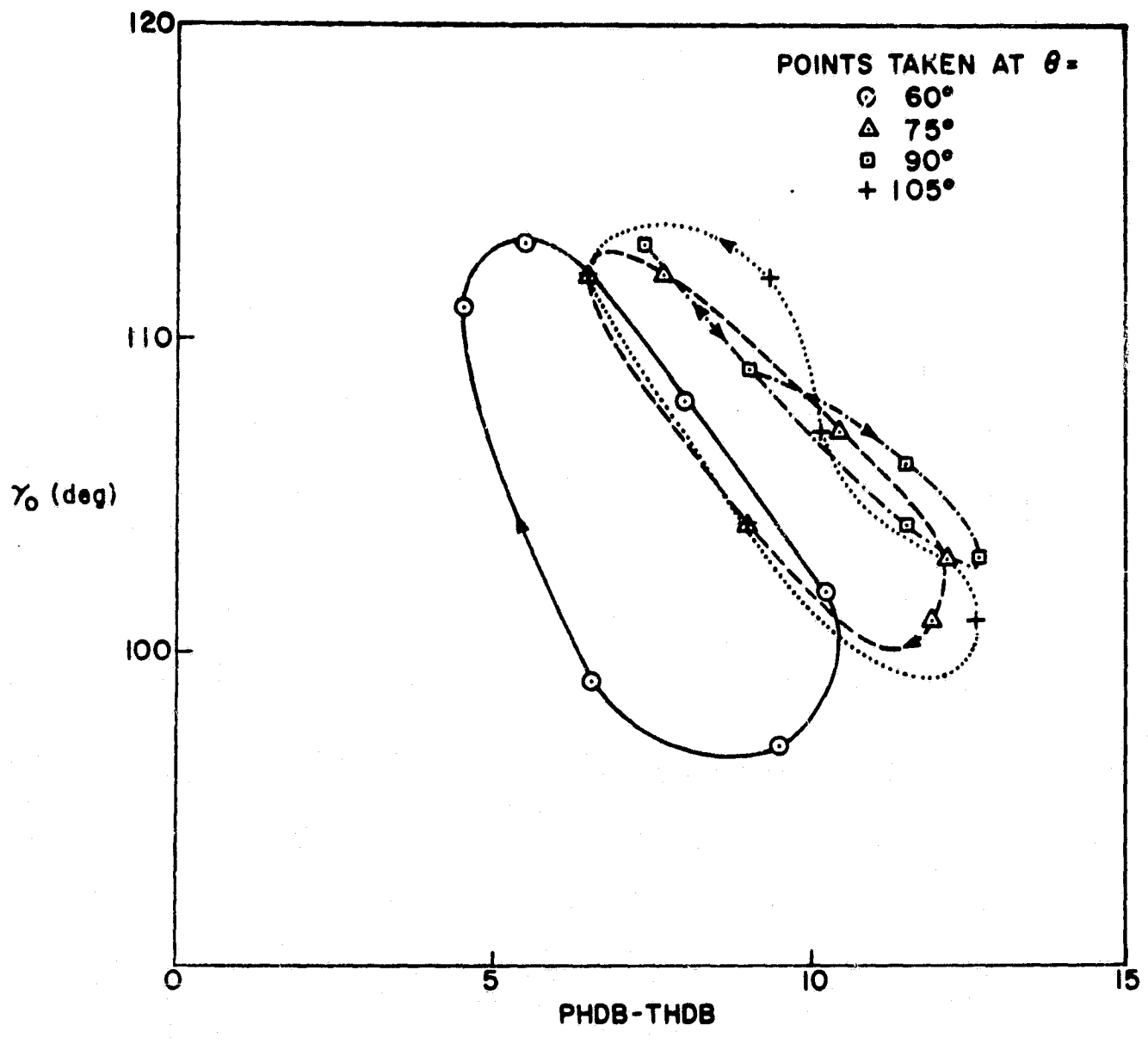


Fig. 33. γ_0 VS θ MINUS θ LINEAR POWERS IN DECIBELS FOR THE IDEAL MODEL. γ_0 traces out an irregular curve as the spacecraft rotates on its axis.

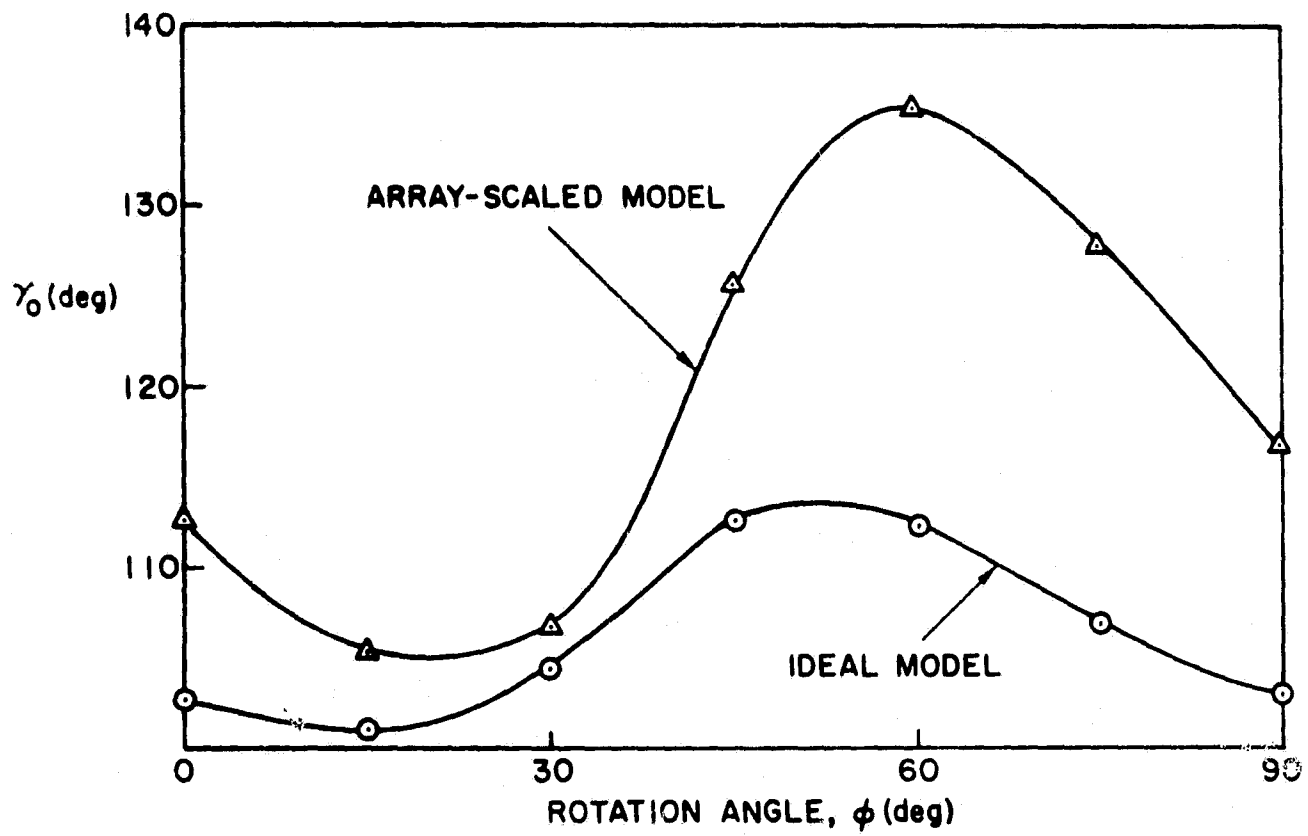


Fig. 34. VARIATIONS IN γ_0 AS THE SPACECRAFT ROTATES OVER 90° . The observation angle is $\theta = 75^\circ$.

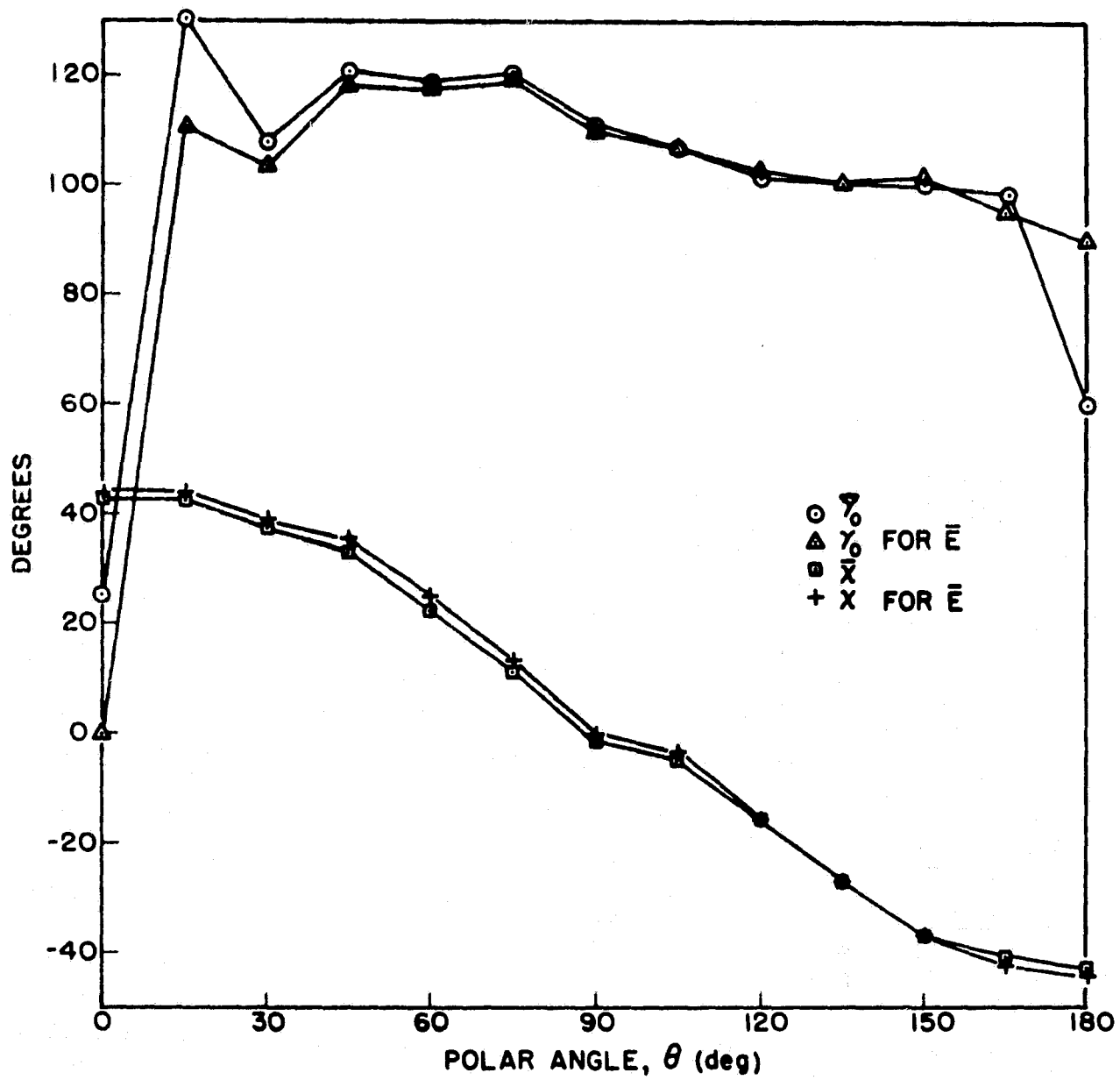


Fig. 35. AVERAGE POINCARÉ PARAMETERS AND POINCARÉ PARAMETERS FOR AVERAGE FIELDS. Averages are over 360° of spacecraft rotation.

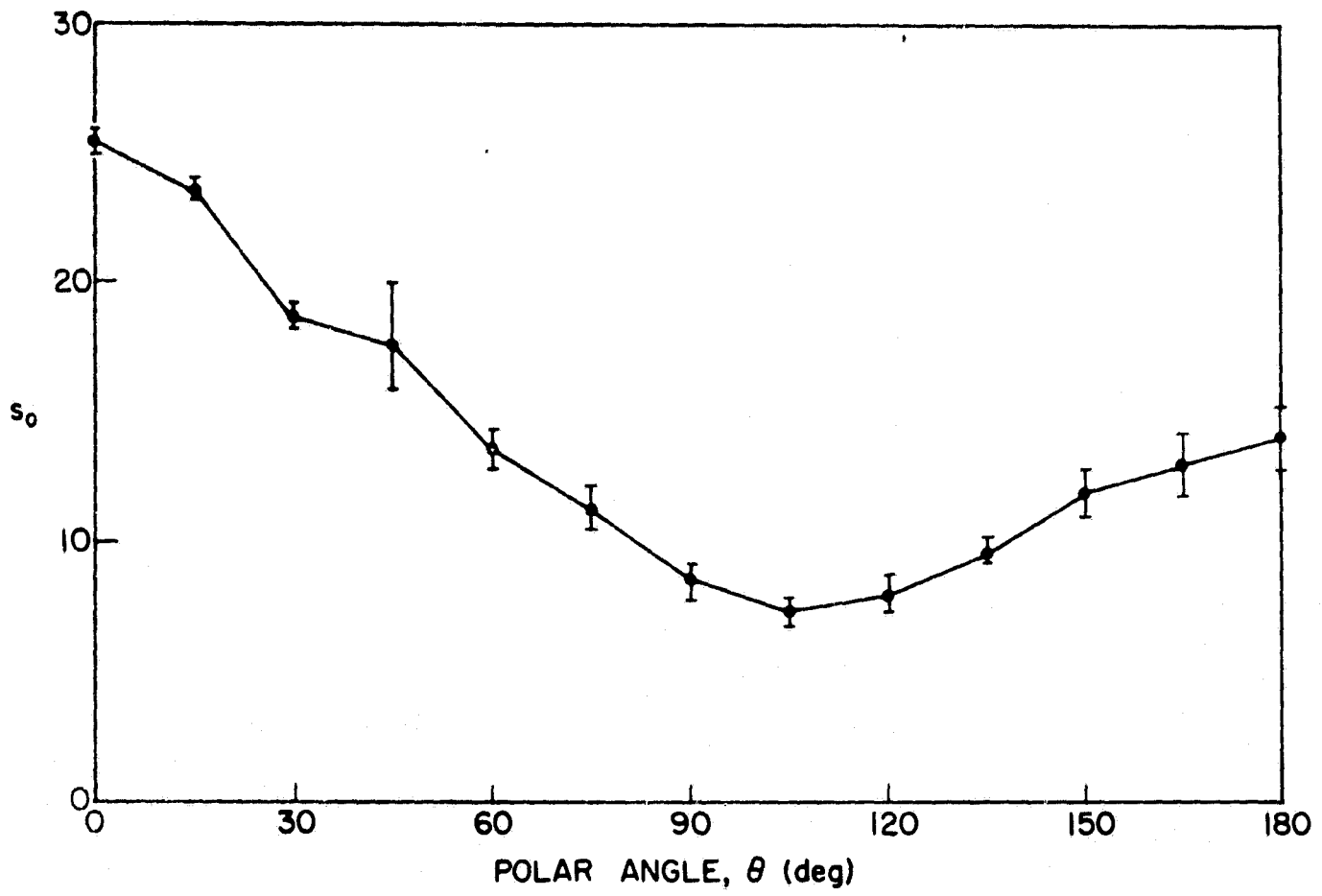


Fig. 36. AVERAGE s_0 OVER 360° OF ROTATION WITH ERROR BARS INDICATING THE MAXIMUM DEVIATION FROM THIS VALUE WHEN AN AVERAGE OVER ONLY 150° IS TAKEN.

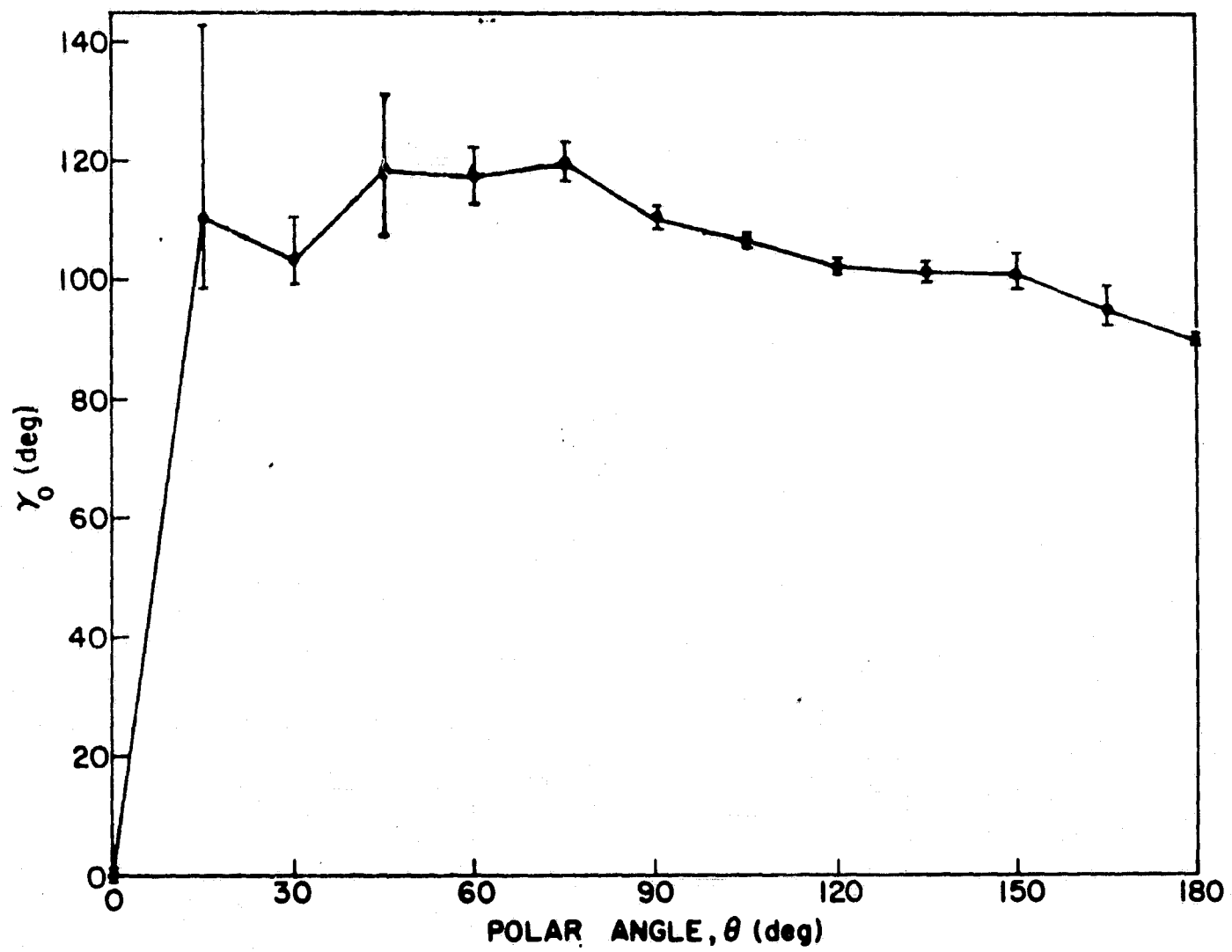


Fig. 37. AVERAGE γ_0 OVER 360° OF ROTATION SHOWING DEVIATION WHEN 150° AVERAGE IS USED.

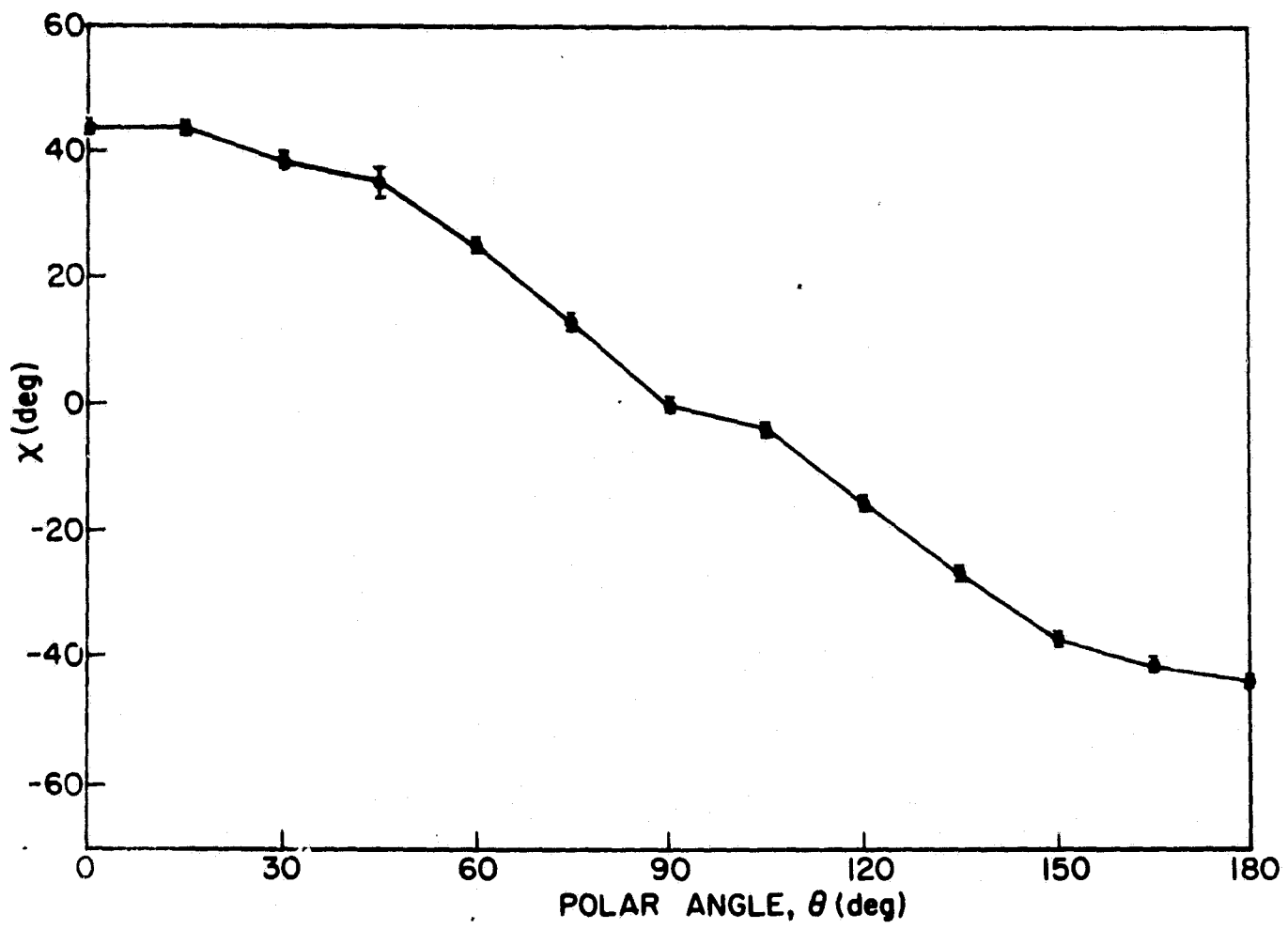


Fig. 38. AVERAGE χ OVER 360° OF ROTATION SHOWING DEVIATION WHEN 150° AVERAGE IS USED.

BIBLIOGRAPHY

- Campbell, M. J., J. Ulrichs, B. W. Hapke (1969), The Electrical Properties of Rocks and Their Significance for Lunar Radar Observations, Technical Report 333, Center for Radiophysics and Space Research, Cornell University, New York.
- Fjeldbo, G. (1964), Bistatic-Radar Methods for Studying Planetary Ionospheres and Surfaces, Ph.D. Dissertation, Stanford University, Stanford, California.
- Hagfors, T. (1961), Some Properties of Radio Waves Reflected from the Moon and Their Relation to the Lunar Surface, *J. Geophys. Res.*, 66, No. 3, 777-785.
- Hagfors, T. (1966), Relationship of Geometric Optics and Auto-Correlation Approaches to the Analysis of Lunar and Planetary Radar, *J. Geophys. Res.*, 71, No. 2, 379-383.
- Hagfors, T. (1968), Chapter IV, in Radar Astronomy, ed. J. V. Evans and T. Hagfors, (McGraw-Hill, New York).
- Kraus, J. D. (1950), Antennas, (McGraw-Hill, New York).
- Middleton, D. (1960), Statistical Communication Theory, (McGraw-Hill, New York).
- Scheuer, P. A. G. (1962), On the Use of Lunar Occultations for Investigating the Angular Structure of Radio Sources, *Australian J. of Physics*, 15, 333-343.
- Tyler, G. L. (1968a), Brewster Angle of the Lunar Crust, *Nature*, 219, 1243-1244.
- Tyler, G. L. (1968b), Oblique-Scattering Radar Reflectivity of the Lunar Surface: Preliminary Results from Explorer 35, *J. Geophys. Res.*, 73, 7609-7620.
- Tyler, G. L. (1968c), The Calculation of Orbitally Determined Experimental Parameters for Bistatic-Radar Observations of Explorers XXXIII and XXXV from Classical Orbital Elements, Tech. Rpt. No. 3609-2, NAS 5-9347, SU-SEL-68-059, Stanford Electronics Laboratories, Stanford, California.
- Tyler, G. L. (1968d), A Dual Polarization Bistatic-Radar Receiving System for Explorers XXXIII and XXXV, Tech. Rpt. No. 3609-3, NAS 5-9347, SU-SEL-68-008, Stanford Electronics Laboratories, Stanford, California.
- Tyler, G. L., V. R. Eshleman, G. Fjeldbo, H. T. Howard, A. M. Peterson (1968), Bistatic Radar Detection of Lunar Scattering Centers with Lunar Orbiter I, *Science*, 157, 193-195.

Tyler, G. L. (1969), Digital Spectral Analysis of Bistatic-Radar Echoes from Explorer XXXV, Stanford University, Stanford Electronics Laboratories Technical Report (in press).

Tyler, G. L., R. A. Simpson (1970), Bistatic Radar Measurements of Topographical Variations in Lunar Surface Slopes with Explorer XXXV, Radio Science (to appear February 1970).

Yakovlev, O. I., A. E. Efimov, S. S. Mamyugov (1968), On Scattering of Meter Radio Waves by the Surface of the Moon, Cosmic Research, VI, 3 (in Russian).